JGR Solid Earth

RESEARCH ARTICLE
10.1029/2025JB031559

Analysis of Seismic Wave Amplification in Sedimentary Basins Using 3D Wavefield Simulations: Nenana Basin, Central Alaska

Yuan Tian[1,2] **and Carl Tape**[2]

[1]Lawrence Livermore National Laboratory, Livermore, CA, USA, [2]University of Alaska Fairbanks, Fairbanks, AK, USA

Key Points:

- Nenana basin, central Alaska, is used to investigate seismic wave amplification for locally recorded earthquakes
- Basin effects are examined by performing wavefield simulations in four different models for 10 earthquakes
- Amplification increases linearly with depth-to-basement, then flattens with a value that depends on frequency and ground motion component

Supporting Information:

Supporting Information may be found in the online version of this article.

Correspondence to:

Y. Tian,
tian7@llnl.gov

Citation:

Tian, Y., & Tape, C. (2025). Analysis of seismic wave amplification in sedimentary basins using 3D wavefield simulations: Nenana Basin, central Alaska. *Journal of Geophysical Research: Solid Earth*, *130*, e2025JB031559. https://doi.org/10.1029/2025JB031559

Received 13 MAR 2025
Accepted 26 OCT 2025

Author Contributions:

Conceptualization: Yuan Tian, Carl Tape
Data curation: Yuan Tian
Formal analysis: Yuan Tian
Funding acquisition: Carl Tape
Investigation: Yuan Tian
Methodology: Yuan Tian, Carl Tape
Project administration: Carl Tape
Software: Yuan Tian, Carl Tape
Supervision: Carl Tape
Validation: Yuan Tian
Visualization: Carl Tape
Writing – original draft: Yuan Tian, Carl Tape
Writing – review & editing: Yuan Tian, Carl Tape

Abstract We investigate seismic wave amplification in Nenana basin, central Alaska, using 3D seismic wavefield simulations. We quantify frequency-dependent amplification by comparing synthetic seismograms among four different seismic velocity models: (a) a tomographic model, (b) a tomographic model with the uppermost 6.5 km replaced by a 1D basin profile, (c) a tomographic model with an embedded ellipsoidal basin, and (d) a tomographic model with an embedded realistic basin. For each model we perform wavefield simulations accurate up to 2 Hz for a set of 10 different earthquakes, which provide a range of frequencies and incident angles for waves interacting with the basin. Average amplification ratios are four on the horizontal components and seven on the vertical component. The dominant influence of the amplification is the 3D geometry of the basin, not the slow-velocity profile near the surface. Our synthetic amplification ratios are in general agreement with amplification estimates obtained from 14 stations that recorded the same set of earthquakes. Our approach offers a general strategy for documenting frequency-dependent basin amplification for a region with realistic basin structures and local earthquakes.

Plain Language Summary Sedimentary basins are regions containing thick layers of sediments and sedimentary rock. Sedimentary basins can trap and amplify seismic waves, leading to stronger and longer shaking during earthquakes. Understanding how this happens is important for studying earthquake behavior and for assessing risks to people and infrastructure. Our study focuses on Nenana basin in central Alaska, a region containing 14 seismic stations and experiencing a variety of different earthquakes. We perform computer simulations of seismic waves to demonstrate how waves are amplified by Nenana basin. By comparing the computer simulation results with real earthquake data, we establish a general approach to understanding basin amplification of seismic waves.

1. Introduction

It is well known—from observations and modeling—that sedimentary basins amplify and prolong ground shaking from earthquakes. Examples include shaking in Mexico City during the 1985 M_w 8.0 Michoacán earthquake (Anderson et al., 1986; Bard et al., 1988; Mayoral et al., 2019), in southern California in 1994 (Bonilla et al., 1997; R. W. Graves et al., 1998), in Kobe, Japan, in 1995 (Furumura & Koketsu, 1998), and in Nepal in 2015 (Galetzka et al., 2015; Oral et al., 2022). These earthquakes caused destruction and loss of life, underscoring the importance of understanding how seismic waves interact with sedimentary basins and the urban structures they contain.

Modeling the effects of sedimentary basins on seismic waves has evolved from theoretical models in the 1980s (Bard & Bouchon, 1980) to 2D wavefield simulations (Bard & Bouchon, 1985; Bard et al., 1988) to 3D wavefield simulations in the 1990s (Frankel, 1993; Furumura & Koketsu, 1998; R. W. Graves et al., 1998; Olsen et al., 1995; Sánchez-Sesma & Luzón, 1995), which were enabled with the expansion of high-performance computing (Komatitsch et al., 2002). Over the past three decades, there have been several studies using 3D wavefield simulations and focusing on specific basins, such as Los Angeles (Day et al., 2008; Komatitsch et al., 2004; Olsen, 2000; Olsen et al., 2003), Mexico City (Cruz-Atienza et al., 2016), Seattle (Frankel et al., 2009), Taipei (Lee et al., 2008), and Osaka (Asano et al., 2016). There are several challenges common to studies of 3D wavefield simulations in sedimentary basins. First, the relevance of the wavefield simulations is limited by the accuracy of the 3D velocity model that describes the basin. Only some basin models benefit from industry data (active-source and well logs) (e.g., Shaw et al., 2015; Süss & Shaw, 2003) or dense station coverage (e.g., Villa et al., 2023; Wang et al., 2021). Furthermore, to capture the highest frequencies in the wavefield, the subsurface

stochastic heterogeneity and viscoelastic attenuation need to be taken into account (R. Graves & Pitarka, 2016; Olsen et al., 2003; Savran & Olsen, 2016), and these are generally not well known. Near-surface soil properties, including complex rheological models, are also needed to model site effects for the high frequencies (Kawase, 2003).

A second challenge in simulation-based modeling of sedimentary basins is that there may not be many ground motion recordings capturing the frequency range of interest. A single large local earthquake produces high-amplitude ground motions and will provide the basin response for that one earthquake (Galetzka et al., 2015), but not the basin response to all earthquakes. In the decades to centuries between major earthquakes, there may not be enough moderate events to be recorded within the basin. Furthermore, there may not be enough stations within the basin to capture the details of the seismic wavefield. Although earthquake recordings are not required for a numerical study, they do provide essential information to assess the validity of the numerical simulations. A third challenge is that there is always a computational limit for the highest frequencies, with each doubling of desired maximum frequency (e.g., 1 to 2 Hz) resulting in a 16-fold increase in computational cost, especially for sedimentary basins that have very low shear wave velocities.

In this study, we examine the amplification of seismic waves in Nenana basin, central Alaska (Figure 1). This study region has several advantages. First, there exists a sedimentary basement model derived from industry data (PRA, 2017; Van Kooten et al., 2012). Second, there are several recent moderate M_w 3–5 earthquakes below or near the basin. Third, there were several seismic stations installed in the basin for a 5-year period (Figure 1), leading to a data-driven characterization of the basin response, including a catalog of estimated moment tensors (Smith et al., 2023). Finally, there is a possibility of the basin experiencing large local earthquakes. The fault zone associated with the basin produced a M_w 6.0 earthquake in 1995 and is likely capable of producing a M_w 7 earthquake (Tape et al., 2015). In the vicinity of the basin, the fault zone is expressed as seismic lineaments at 15–25 km depth (Sims et al., 2025), and it is unknown if a large rupture would extend into the basin itself.

We perform a suite of 3D seismic wavefield simulations for a set of 10 earthquakes and four seismic velocity models. The models include adaptations of a tomographic model (Berg et al., 2020) and a detailed model of Nenana basin, with the purpose of examining the influence of the slow velocities and geometric boundaries (lateral and depth) of the sedimentary basin. With the advantage of recorded data for these events, we are able to provide a systematic data- and simulation-driven approach to document the frequency-dependent and depth-dependent effects of basin structure on amplification of the local seismic wavefield. Our focus is on frequencies $\lesssim$2 Hz.

Our study builds upon previous efforts using recorded observations and wave propagation methods to quantify basin amplification. We build upon the approaches of Olsen (2000) and Day et al. (2008), who performed wavefield simulations of local earthquakes to quantify frequency-dependent amplification effects in Los Angeles basin. Focusing on a region in central Alaska, our main extension from these efforts is to consider four related velocity models—including ones with or without the basin—allowing us to quantify frequency-dependent basin amplification for different pairs of velocity models. Furthermore, we simulate real local earthquakes, enabling comparison of simulation results with observations. We find that amplification within Nenana basin occurs primarily from surface wave reverberations caused by the velocity contrast at the lateral boundaries of the basin.

2. Methods

We examine 10 local earthquakes from the study by Smith et al. (2023), who quantified seismic basin amplification in Nenana basin for a set of 43 local, regional, and teleseismic earthquakes. The 10 earthquakes, having magnitudes M_w 3.7–4.3, are displayed in Figure 1a and listed in Table 1.

2.1. Velocity Models

We consider four velocity models in this study:

M1. The tomographic model of Berg et al. (2020), specifically, the 200 km by 150 km subregion containing Nenana basin. Berg et al. (2020) used Rayleigh wave phase velocities, Rayleigh wave H/Z ratios, and receiver functions to constrain the crustal and uppermost mantle structure. The velocity model at 1 km depth (Figure S1 in Supporting Information S1) shows the signatures of many basins in Alaska, including Nenana basin. The tomographic model has a relatively coarse horizontal discretization of 0.1° (11 km) in latitude and

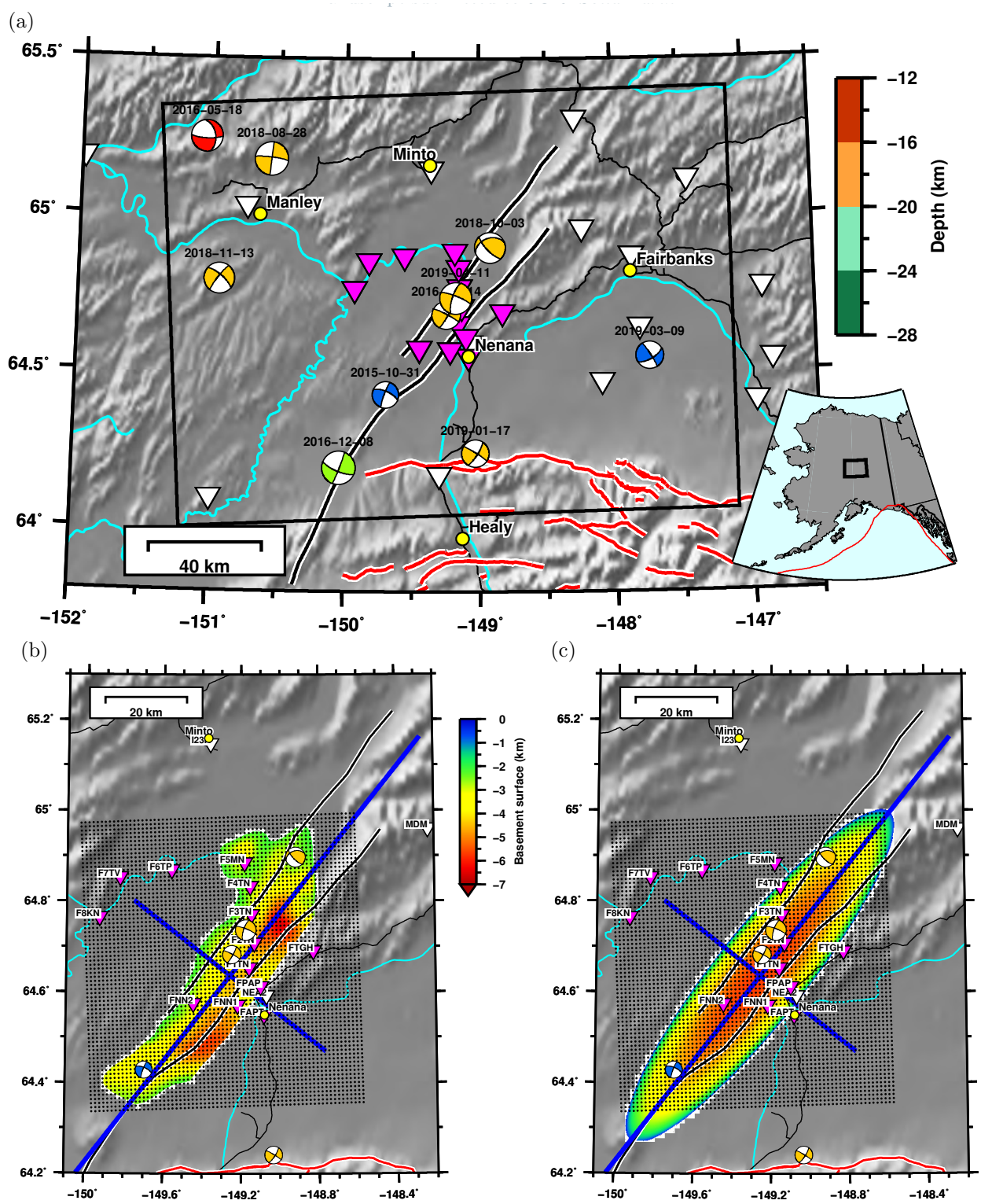

Figure 1. Study region of Minto Flats and Nenana basin, central Alaska. (a) Earthquake sources and stations used in this study. The 10 events are depicted as beachball focal mechanisms, colored by depth (Table 1). The stations are depicted as inverted triangles: white for the permanent network and magenta for the FLATS network (Tape et al., 2018). Active faults are red (Koehler et al., 2012); the two lineaments of the Minto Flats fault zone are black (Tape et al., 2015). The black box shows the domain of the 3D wavefield simulations. (b) Nenana basin basement map (PRA, 2017), colored by depth. The two cross-section profiles depicted by blue lines correspond to Figure 2. The dense grid depicted by black dots of 4,896 synthetic stations (72 × 68) is used to quantify the impact of basin structures on ground motion amplification.

Table 1
Earthquakes Used in This Study and Displayed in Figure 1

Origin time	Longitude (°)	Latitude (°)	Magnitude (M_w)	Depth (km)	Distance to basin (km)	Azimuth (°)
2015-10-31 02:56:35.57	−149.6969	64.4285	3.40	25	31	176
2016-01-14 19:04:10.73	−149.2479	64.6827	3.70	17	5	34
2016-05-18 03:25:48.32	−151.0651	65.2466	4.10	12	109	89
2016-12-08 10:18:13.87	−150.0376	64.1937	4.35	21	62	180
2018-08-28 15:18:43.46	−150.5718	65.1780	4.30	16	87	83
2018-10-03 03:29:37.54	−148.9191	64.8979	4.00	19	33	9
2018-11-13 15:26:41.91	−150.9466	64.7938	3.95	16	82	115
2019-01-17 12:13:55.49	−149.0340	64.2410	3.55	17	45	128
2019-03-09 23:39:58.33	−147.7368	64.5498	3.60	26	73	59
2019-04-11 10:42:45.61	−149.1761	64.7370	4.15	17	12	19

Note. These are a subset of events from Smith et al. (2023). The distance-to-basin and source azimuth are calculated with respect to longitude −149.26° latitude 64.65°.

0.2° (9.7 km) in longitude, and a finer depth discretization that varies from 0.25 km at the surface to 0.5 km at 3 km depth and 1 km at 5 km depth.

M2. M1 with the uppermost 6.5 km replaced with a 1D basin profile.

M3. M1 with an embedded ellipsoidal basin (Figure 1c) filled with a 1D basin profile. The ellipsoidal shape is a least-squares best-fitting shape to the realistic basin (M4).

M4. M1 with an embedded realistic basin (Figure 1b) filled with the 1D basin profile. The basin geometry is from PRA (2017), extended to the southwest by the model of Dixit et al. (2017). It is realistic in the sense that it was derived from industry data in the region, including geophysical well logs and 3D active-source seismic surveys.

Guided by our modeling objectives, we make two modifications to the realistic sedimentary basement surface of PRA (2017). Our finite-element mesh, which will be discussed in Section 2.2, is designed to accommodate low wavespeed values within the basin, but it is not designed to conform to the basement surface, such as in Stupazzini et al. (2009). Also, the mesh is not designed to accommodate structures that influence waves having higher frequencies than 2 Hz. To ensure that the basin features are accurately handled by the mesh, we first smooth the original basement surface, which has a discretization of 300 m, by using Gaussian smoothing with a 2.9 km length scale. Finally, due to the uncertainty associated with the lateral boundaries of the basement surface, we remove all portions of the basement surface that have a basement depth shallower than −2 km elevation, as shown in Figure 1b.

The 1D basin profile is derived from active source and well log data in the region. Below a depth of 4.5 km, the 1D basin profile is the generic basin profile of Brocher (2008), which is based on industry measurements (V_P logs and active source imaging) in California geological units. Near the surface, the basin profile is slightly slower than the generic Brocher basin profile. Values at the surface of the Nenana basin model are $V_P = 2082$ m/s and $V_S = 664$ m/s, compared with $V_P = 2240$ m/s and $V_S = 778.9$ m/s for Brocher.

Cross sections of these models are shown in Figure 2, and depth profiles for one example location are shown in Figure 3. The profiles convey that the 1D basin model (used in M2, M3, M4) is much slower than the tomographic model: within the upper 4 km, the realistic basin (M4) is, on average, 53% slower (0.85 km/s) than the tomographic model (M1). Furthermore, the profiles display the sharp contrast at the bottom of the basin, where the velocities of the embedded basin model step to the higher velocities of the tomographic model. We can also compare the velocity models for any given longitude-latitude location. Figure 3 shows a comparison at the location where the realistic basin (M4) has its maximal depth of 6.5 km. For the chosen longitude-latitude point of the profile in Figure 3, the ellipsoidal basin (M3) depth is 1.25 km shallower than the realistic basin (M4).

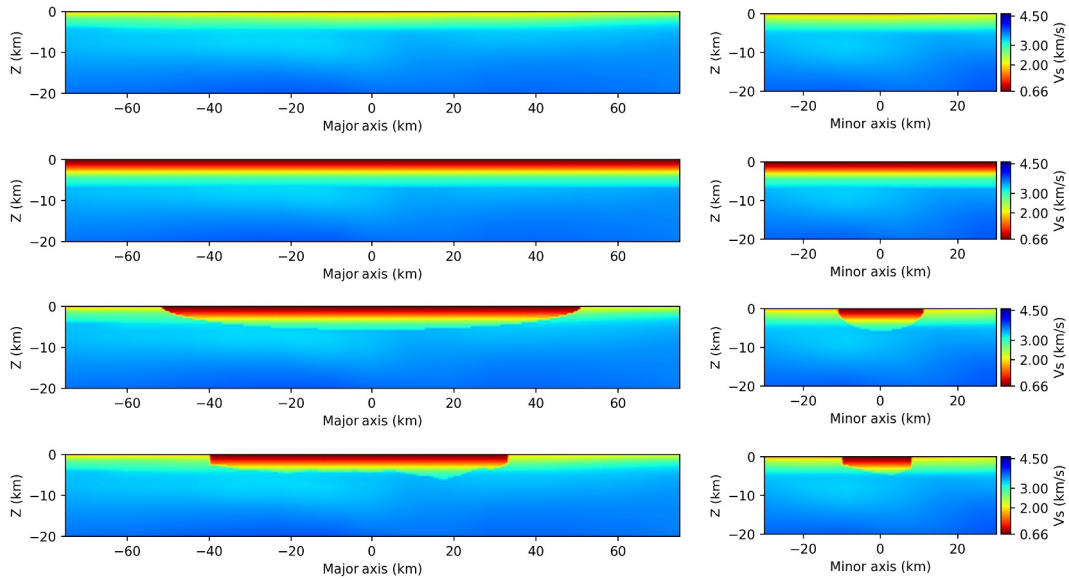

Figure 2. Cross sections of four seismic velocity models used in this study (Section 2.1). From top to bottom, they are M1: Berg et al. (2020), M2: M1 with a 1D slow model for the uppermost 6.5 km, M3: an ellipsoidal basin model embedded in M1, and M4: a realistic basin model embedded in M1. The locations of the two cross sections are shown in Figures 1b and 1c.

2.2. 3D Wavefield Simulations

We use the open-source spectral-element method wave propagation solver Specfem3d for constructing the mesh and performing wavefield simulations (Komatitsch et al., 2004).

The minimum shear velocities in the four models (Figure 2) are 1332 m/s (M1) and 664 m/s (M2, M3, M4). For M2–M4, the minimum velocity is the 1D basin velocity value at 0 m depth. For M1, the minimum velocity is from Berg et al. (2020) for a point that happens to be west of Nenana basin (see Figure S1c in Supporting Information S1). We are interested in calculating numerically accurate synthetic seismograms up to frequencies of 2 Hz. The choice of frequency, combined with the minimum shear velocities, guide our construction of the finite-element mesh. Our mesh has 4,890,624 elements and is displayed in Figure S3 in Supporting Information S1. Each element has five Gauss-Lobatto-Legendre (GLL) points along the x, y and z directions, resulting in a total of 328,078,080 global gridpoints.

We run the python package wfdiff to calculate the minimum resolvable period of our mesh. wfdiff inputs two sets of seismograms, with one set obtained using a finer mesh than the other set. We achieve this by performing one simulation with the standard five GLL points and a second simulation using seven GLL points, resulting in a finer mesh. The finer mesh requires reducing the time step by a factor of about two, which in turn requires calculating more time steps to achieve the same length of synthetic seismograms. Overall, the GLL 7 simulation is about 16 times the computational cost of the GLL 5 simulation (8x for the finer spatial grid and 2x for the shorter time step). By comparing the two sets of synthetic seismograms for the same velocity model, we can quantify the minimum resolvable period of the coarser (GLL 5) set of seismograms.

An example calculation of the minimum resolvable period is shown in Figure S4 in Supporting Information S1. For this velocity model (M4), this event (2018-10-03), this basin station (F5MN), and this component (E), the minimum resolvable period is 0.36 s (2.8 Hz). Based on a larger set of similar calculations (Tian & Tape, 2025a), we find that the synthetic seismograms within the lowest-velocity regions of the basin are resolved up to 2 Hz, with non-basin stations resolved up to 4 Hz and higher.

We save the seismic wavefield time series at a dense grid of synthetic stations, in addition to the locations of 22 real stations (Figure 1a), 13 of which are FLATS stations that were deployed between 2014 and 2019. The synthetic grid contains $72 \times 68 = 4896$ stations spaced apart by 1 km (Figure 1b). A typical wavefield simulation of 300 s of seismograms takes about 3.3 hr on 192 cores (634 CPU-hours) of the HPC cluster at UAF. The total number of simulations performed is 40 (=4 models $\times$ 10 events).

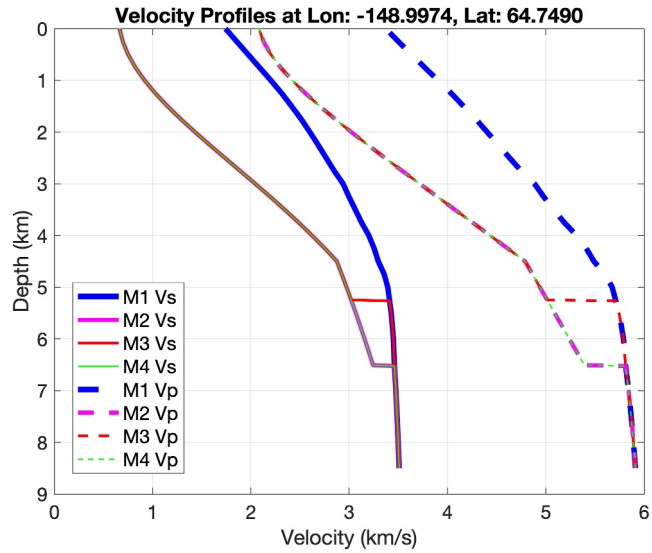

Figure 3. Depth profiles of V_S and V_P for four models in this study (Figure 2). The profile is taken at the location of the maximum depth of the realistic basin model (M4), which is 6.5 km. At this location, the ellipsoidal basin (M3) depth is 1.25 km shallower than the realistic basin (M4). Both M3 and M4 contain the generic basin profile above the basement surface, whereas M1 is the Berg et al. (2020) tomographic model, which is considerably faster. At this location, the profile for M2 is identical to M4. See Figure S2 in Supporting Information S1 for a comparison with three other profiles from different locations.

2.3. Calculating Spatial-Dependent Amplification

The synthetic grid of stations enables us to view synthetic patterns of ground motion that are not possible with real stations, given the sparse and irregular coverage. Figure 4, which will be discussed further in Section 3.1, displays wavefield peak amplitudes for all 4,896 stations in the synthetic grid. Spatial maps of basin amplification, such as we will see in Figure 11, provide a natural view of amplification for comparison with the provided basin structure (Figure 1). These maps require specification of the frequencies used to calculate the amplification, discussed next.

2.4. Calculating Frequency-Dependent Amplification

Figure 5 provides an example for how we calculate the amplification of ground motion for one source-station pair for two models. Here the source is chosen from Table 1, and the station location is F4TN, which is inside the realistic basin model (M4: Figure 1b). The two models for comparison are M1 and M4, which allow us to examine the influence of a realistic basin model embedded within a 3D tomographic model.

We then calculate amplitude spectra for the two seismograms (for M1 and M4), as shown in Figure 5b, and then the amplification ratio (Figure 5c). In this example, the amplification ratio is approximately 11 for frequencies $\geq$0.25 Hz. By applying the procedure in Figure 5 to the subset of synthetic stations inside the lateral boundaries of the basin—whether it is the realistic basin (Figure 1b) or the idealized ellipsoidal basin (Figure 1c)—we can isolate the wavefield effects within the basin. There are 1,696 synthetic basin stations in M3 (Figure 1c) and 1,298 basin stations in M4 (Figure 1b).

Figure 6 distills a set of 10 events × 1,696 amplification spectra, each like Figure 5c, into a single amplification spectrum (in this case, Z-component) that is representative of the basin model (in this case, M3). For each event, we calculate the median spectrum over all 1,696 synthetic grid stations that are inside the basin. Then, from the set of 10 spectra, we calculate a median spectrum, as well as the median absolute deviation among the 10 spectra.

2.5. Emphasis on Low-Frequency Amplification

To distill the spectrum of amplitude ratios into a subset of quantities, we define a range of frequencies over which we calculate a median value. We choose a frequency range of 0.1–0.5 Hz, because it provided the best

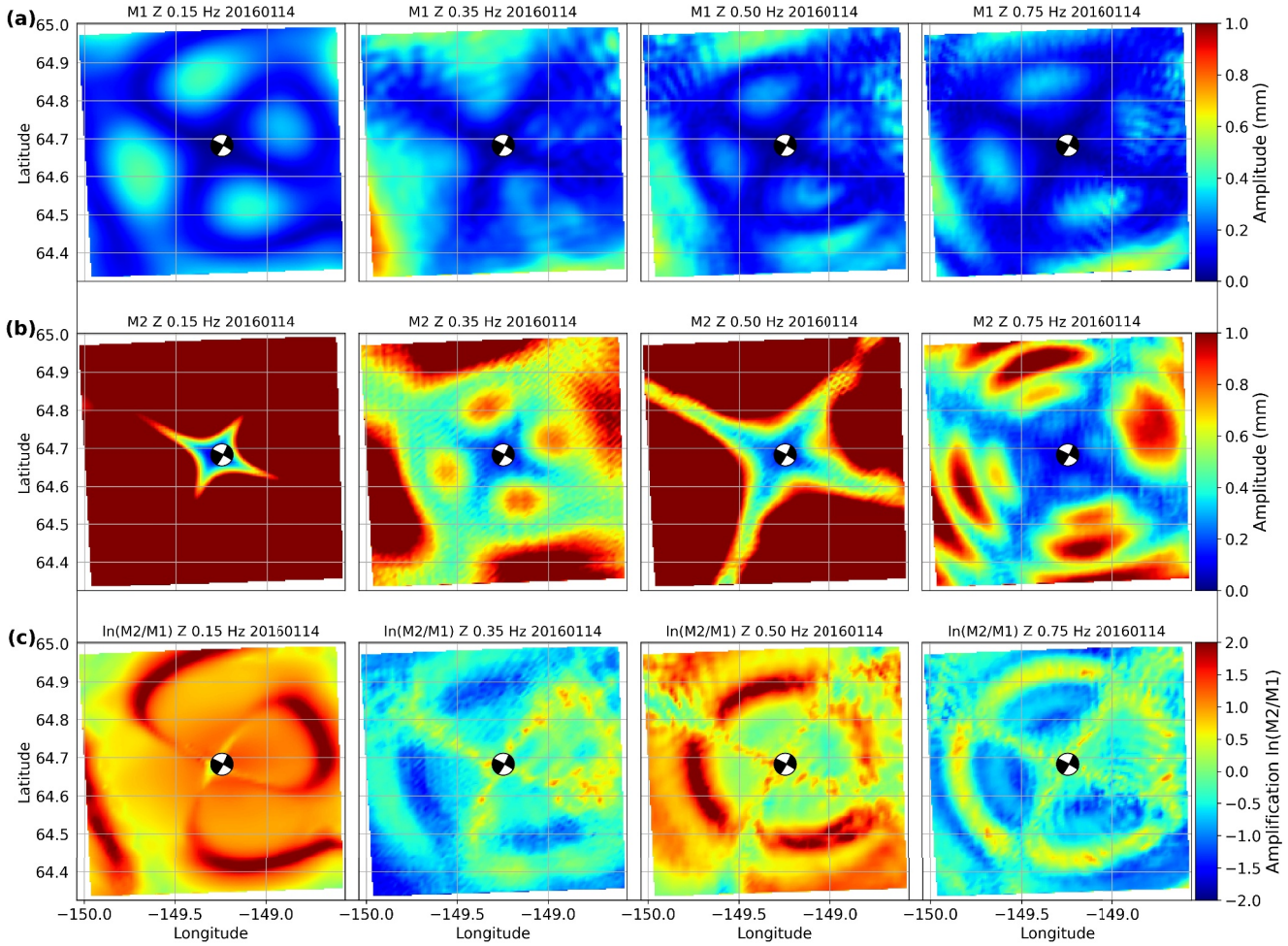

Figure 4. The dependence of amplification maps on source radiation and on frequency, shown for wavefield simulations of an event on 2016-01-14 at 17 km depth and having a strike-slip mechanism. The vertical component of displacement is displayed for frequencies 0.15 Hz (left column), 0.35, 0.50, and 0.75 Hz. The synthetic grid of stations is shown in Figure 1b. (a) Peak displacement amplitude for model M1. (b) Peak displacement amplitude for model M2. The color scale is saturated in order to have direct comparison with (a). An unsaturated version is displayed in Figure S6 in Supporting Information S1. (c) Amplification ratio ln(M2/M1), with 0.1 representing 10% amplification of M2 with respect to M1. Additional event- and frequency-specific amplification maps can be found in Tian and Tape (2024).

agreement between synthetic calculations of amplification (same station; different velocity models) and the data calculations of amplification (basin station vs. nearby bedrock station) in Smith et al. (2023). While the synthetic seismograms are resolved up to 2.0 Hz, the higher-frequency seismograms warrant additional considerations, such as the source-time function, the reliability of the velocity model, and the influence of anelastic attenuation (Section 4.4).

The example in Figure 5c shows an amplification ratio of $\ln(M3/M1) = 2.1 \pm 0.5$, corresponding to a ratio of 8.4 ± 1.7. Thus, we obtain a single amplification value from the full amplification spectrum for this one event, one station, one component, and chosen frequency range (0.1–0.5 Hz).

2.6. Calculating Depth-Dependent Amplification

Because we know the depth-to-basement for the basin models we use, we can examine how amplification varies as a function of the basin depth below each station. This requires partitioning the stations into depth bins (e.g., 0–0.5 km, 0.5–1.0 km, etc) and then aggregating the frequency-dependent amplification ratios for one or more events.

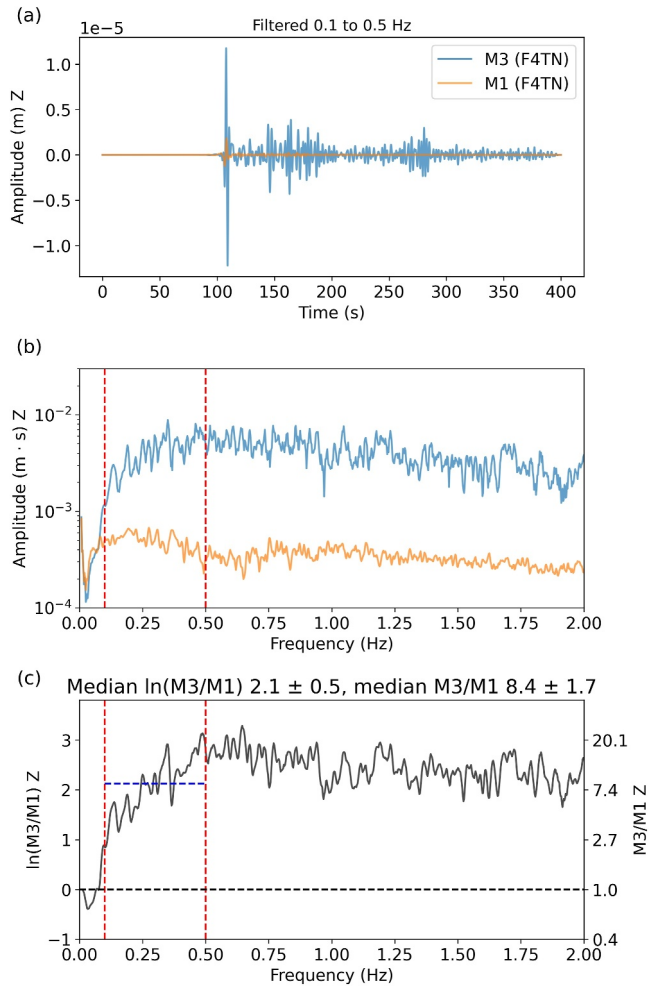

Figure 5. Example calculation of frequency-dependent amplification for a pair of synthetic seismograms computed using two different 3D models, M1 and M3. Model M1 is Berg et al. (2020), and Model M3 is Berg et al. (2020) plus an embedded ellipsoidal basin model (Figure 2). The event is 2016-01-14 M_w 3.70 (Table 1). The station is F4TN (Figure 1b). The bandpass filter used in (a) is 0.1–0.5 Hz and corresponds to the vertical dashed lines in (b) and (c). (a) Vertical-component synthetic seismograms at station F4TN for models M1 (orange) and M3 (blue). The M3 seismogram has much-higher amplitudes and a longer coda. (b) Amplitude spectrum of the two seismograms. The spectra are smoothed with a mean filter having a width of 0.18 Hz. (c) Ratio of spectra shown in (b). The left axis shows ln(M3/M1), while the right axis shows M3/M1. The median amplification over the frequency interval 0.1–0.5 Hz is $\ln(M3/M1) = 2.1 \pm 0.5$, which corresponds to an amplification ratio of $M3/M1 = 8.4 \pm 1.7$.

3. Results

The following subsections provide results based on the methods outlined in Sections 2.3, 2.4, and 2.6.

3.1. Source Effects

The earliest studies of basin amplification represented the incoming waves as plane waves (P, S). However, for local earthquakes in many tectonic settings—including near Nenana basin (Smith et al., 2023)—there are considerable variations in amplitudes due to different source mechanisms and different hypocenters. We considered two approaches to addressing variations due to sources. One approach is to systematically surround the target basin with a dense grid of uniformly spaced sources (Wirth et al., 2019) and then perhaps consider a wide range of uniformly distributed fault planes. The collective results would emphasize features caused by the basin, while minimizing source effects. The second approach, which we take, is to consider a set of actual earthquakes having different depths, distances, and source mechanisms. This has the advantage of enabling

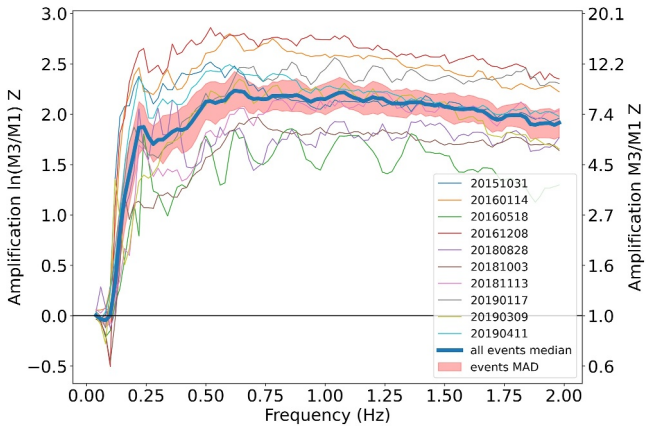

Figure 6. Nenana basin amplification M3/M1 as a function of frequency, shown as the median over all 10 events (Table 1). The basin model featured here is an idealized ellipsoid (Figure 1c). The calculations are performed for all synthetic-grid stations inside the ellipse. The left axis is expressed as ln (M3/M1), the right axis is M3/M1. The thick blue curve is the median over all 10 events; the red swath is ± the median absolute deviation (MAD). A version of this plot appears in Figure 8b. The frequency range 0–0.5 Hz is displayed in Figure 7a.

wiggle-for-wiggle comparisons with real data, with the drawback that the collective results will exhibit stronger source effects than in the first approach.

Figure 4 illustrates the frequency-dependent signature of sources on amplification maps for two velocity models (M1, M2) that do not have a basin model. The example earthquake is an event at 17 km depth (Table 1). We will discuss the left column first, which is based on measurements of synthetic seismograms filtered within a 0.05 Hz narrow band centered at 0.15 Hz. The upper left subplot shows the peak amplitude on the vertical component. The four light-colored quadrants are in the directions of maximum P-wave radiation, both for the Berg et al. (2020) model (M1) and for the shallow-slow-1D model (M2). The M2/M1 amplification map in the lower left subplot contains features from both the M1 and M2 patterns, resulting in a spiral-like pattern that would be difficult to interpret without having the upper subplots.

The overall amplitude of the peak ground motion also depends on frequency. Figure 4b shows that at 0.35 and 0.75 Hz there is relatively low amplitude for model M2, which has a slow 1D model in the uppermost 8 km. This results in the two overall-negative (blue) amplification maps in the bottom row, for 0.35 and 0.75 Hz. We attribute the frequency-dependent oscillations in M2 (and in ln(M2/M1)) to resonance within the M2 slow layer.

Amplification patterns such as those in Figure 4c are not intuitive. They show that significant amplification ratios can occur due to the same source seeing two different structures, neither of which (in this case) involves a basin. By considering a set of events, we are able to document the variability due to the sources, enabling us to quantify the amplification effects due to basin structures.

3.2. Frequency-Dependent Amplification

We are primarily interested in the effects of the basin—not the sources—on the seismic wavefield. Therefore we aggregate results from all 10 events. Figure 6 shows an example of the vertical-component displacement amplification spectra for all 10 events, with the median spectrum (and median absolute deviation) superimposed. The comparison is M3/M1, which shows the influence of an ellipsoidal basin with low seismic velocities (Section 2.1). Two coordinate systems are shown. On the left axis is ln(M3/M1), which can be thought of as percent difference, since $\ln(b - a) \approx (b - a)/a$; a value of 0.1 would be 10% difference. On the right axis is the direct amplification ratio M3/M1.

Figure 6 conveys fundamental information about the basin. Considering all the events, the amplification ratios are 4–16 for 0.2–2.0 Hz, with the median curve having a ratio of about 7. In other words, the displacement inside the basin is about 7 times larger than in the tomographic model of Berg et al. (2020).

Focusing on the lower frequencies (Figure 7), we showcase the "ramp" in amplification that occurs between 0 and 0.25 Hz for the ellipsoidal basin. This ramp is the result of amplification of surface waves. For 1D models and our

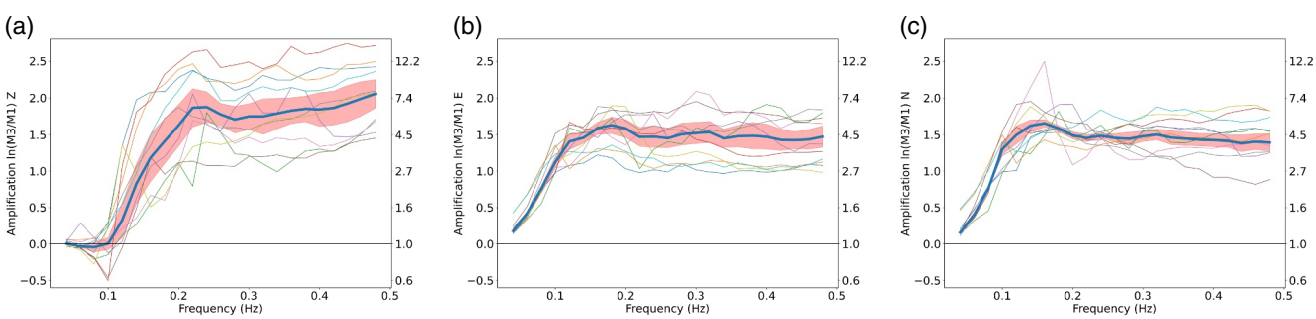

Figure 7. Nenana basin amplification as a function of frequency, displayed for 0–0.5 Hz, for the idealized ellipsoidal basin (M3). (a) Z-component (zoom-in on Figure 6). (b) E-component. (c) N-component. See Figure S9 in Supporting Information S1 for the results for the realistic basin (M4), which are similar.

3D tomographic model (M1), surface waves are the dominant-amplitude waves for regional and local earthquakes for these frequencies. This can be verified by examining the time-dependent polarization of the observed or synthetic three-component seismograms. The ramp in Figure 7 is the result of the changing sensitivity of (incoming) surface waves to the depth of the basin. Below a certain frequency (determined by the depth of the basin), the surface waves are sensitive mostly to sub-basin structure and do not "see" the basin. Above a certain frequency, the surface waves are sensitive to the shallowest structures and do not see the bottom of the basin. The vertical-component results reveal Rayleigh wave amplification reaching a factor of about 7 over the interval from 0.1 to 0.25 Hz (Figure 7a). The horizontal-component results reveal Love wave amplification increasing to a factor of about 5 over the interval from 0 to 0.15 Hz (Figures 7b and 7c).

Figure 8 shows different amplification maps, considering different combinations of models (Section 2.1). The four models enable numerous comparisons and questions:

- M1 versus M2 (Figure 8a). How does adding a shallow layer—without any basin—amplify the wavefield?
- M1 versus M3 (Figure 8b). How does an idealized basin amplify the wavefield?
- M1 versus M4 (Figure 8c). How does a realistic basin amplify the wavefield?
- M2 versus M3 (Figure 8d). How does the geometry of an idealized basin amplify the wavefield? (The velocity model inside the basin is identical in M2 and M3.)
- M3 versus M4 (Figure 8f). How does a realistic basin compare with an idealized basin?

We examined the effects of M2 in Section 3.1. The properties of the 1D shallow model result in low-amplitude peak displacements at frequencies near 0.35 and 0.7 Hz, resulting in the two troughs of deamplification in Figure 8a, as well as the two peaks in M3/M2 (d) and M4/M2 (e). The results in Section 3.1 show that the slow-velocity structures alone—without a basin—do not result in clear amplification across all frequencies.

A comparison of Figures 8b and 8c indicates that the overall pattern of amplification can be represented by an ellipsoidal basin. Although the two basin models are quite different (Figures 1b and 1c), the amplification spectra at 0.05–2 Hz are very similar, as shown in the direct comparison of Figure 8f.

Figures 8d and 8e indicate that the geometry of the basin is the key factor in causing amplification, since both M3 and M4 are amplified relative to a model (M2) having the same inside-basin slow velocities but without any lateral basin boundary. Furthermore, all three models have strong velocity contrasts at depth: 6.5 km everywhere for M2, and the basement surface for M3 and M4. While the plots in Figure 8 aggregate all stations inside the basin, the breakdown by depth-to-basement, next, shows that amplification increases with basin depth.

3.3. Depth-Dependent Amplification

Since we ourselves define the basin models, we know the depth to the base of the basin below each station in the synthetic grid. Figure 9 illustrates the construction of a depth-dependent amplification curve for a fixed frequency of 1.0 Hz. For illustrative purposes, we color each synthetic-grid station according to its underlying basin depth. For example, within the synthetic grid of 4,896 stations, there are 3,200 non-basin stations and 1,696 in-basin stations for the M3 basin model (Figure 9a).

We then calculate the amplification ratio M3/M1 for all 10 events and then plot the median value in the right subplot. We bin these points in $\Delta z = 200$ m intervals and plot the median value. Finally, we fit a simple two-segment, "ramp-plateau" curve to the median points. As shown in the legend of Figure 9a, the best-fitting function has a slope of $k = 1.15\,\mathrm{km}^{-1}$ (shown as the first parameter in the parentheses) and a corner at a depth of 1.4 km. The second number in the parentheses, 1.91, is the height of the plateau (ln(M3/M1) = 1.91, M3/M1 = 6.75) in the fitted function. The third number in the parentheses, 0.34, is the y-intercept (ln(M3/M1) = 0.34, M3/M1 = 1.40) of the fitted function.

The same procedure is then applied to the more realistic basin (Figure 9b). This poses challenges, since the basin boundary is abrupt (by design: Section 2.1) and there are no points in the depth range between 0 and 2 km. For this frequency, the realistic basin model exhibits a slight decrease in amplification (2.1 to 1.9) with increasing depth, starting at about 3 km depth.

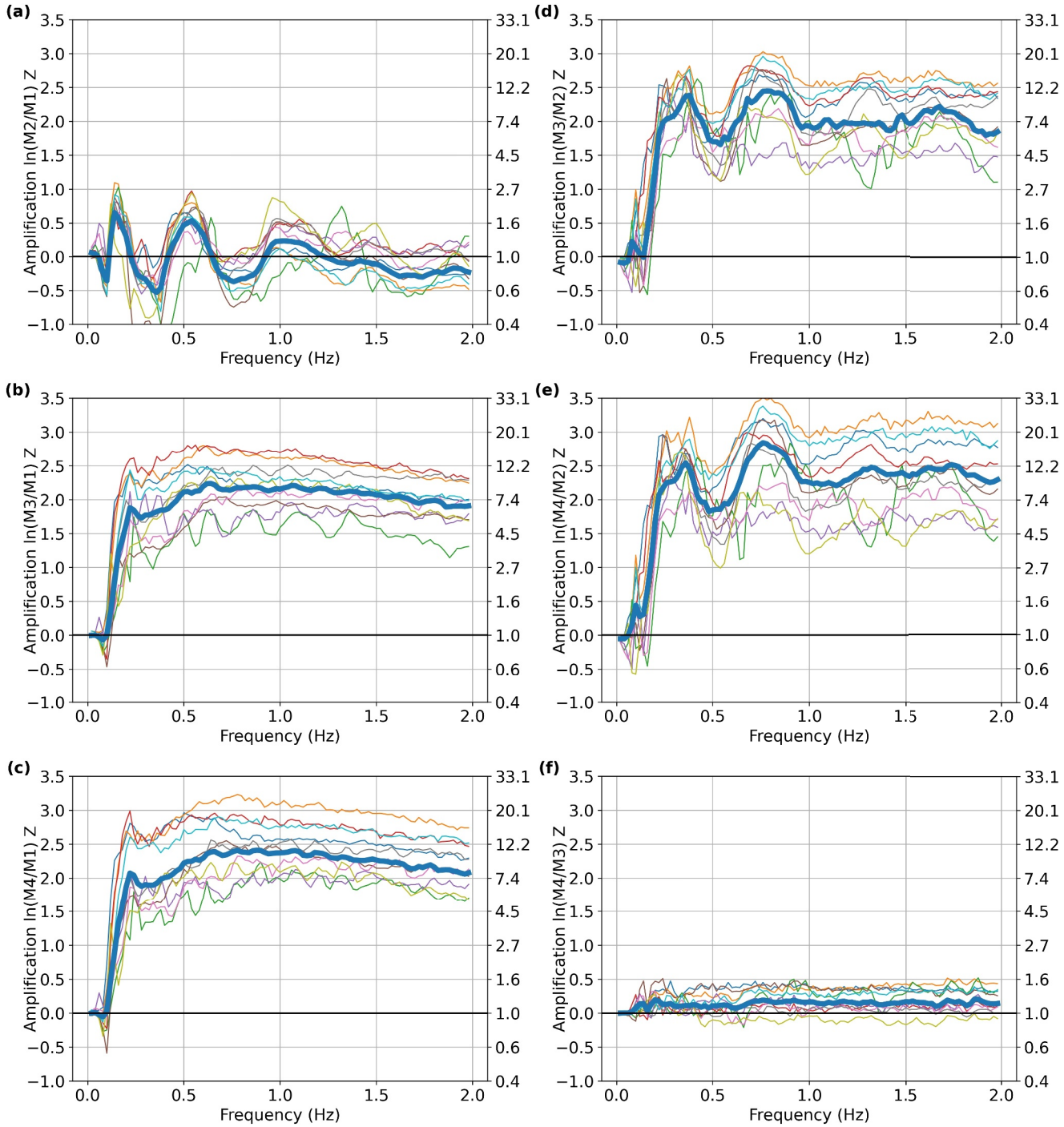

Figure 8. Basin amplification as a function of frequency, shown for the Z component of displacement. Each colored curve is for a different event; see Figure 6 for the legend. The thick blue curve is the median over all 10 events (Table 1). Models M1, M2, M3, and M4 are shown in Figure 2. The number of synthetic stations (out of 4,896 total) used for the calculations is listed in parentheses and depends on the two models being compared. (a) M2/M1 (1128). (b) M3/M1 (1,696). (c) M3/M2 (1,696). (d) M4/M1 (1298). (e) M4/M2 (1298). (f) M4/M3 (1128). The corresponding plots for the E and N components are displayed in Figures S10 and S11 in Supporting Information S1.

Figure 10 displays results for the ellipsoidal model (M3) for all three components and for a set of log-spaced frequencies ranging from 0.01 to 2.0 Hz, corresponding to the period range 0.5–100 s. The jagged curve is the median curve, and the dashed curve is the best-fitting two-segment (ramp-plateau) function. The corresponding plots for the realistic basin (M4) are shown in Figure S14 in Supporting Information S1.

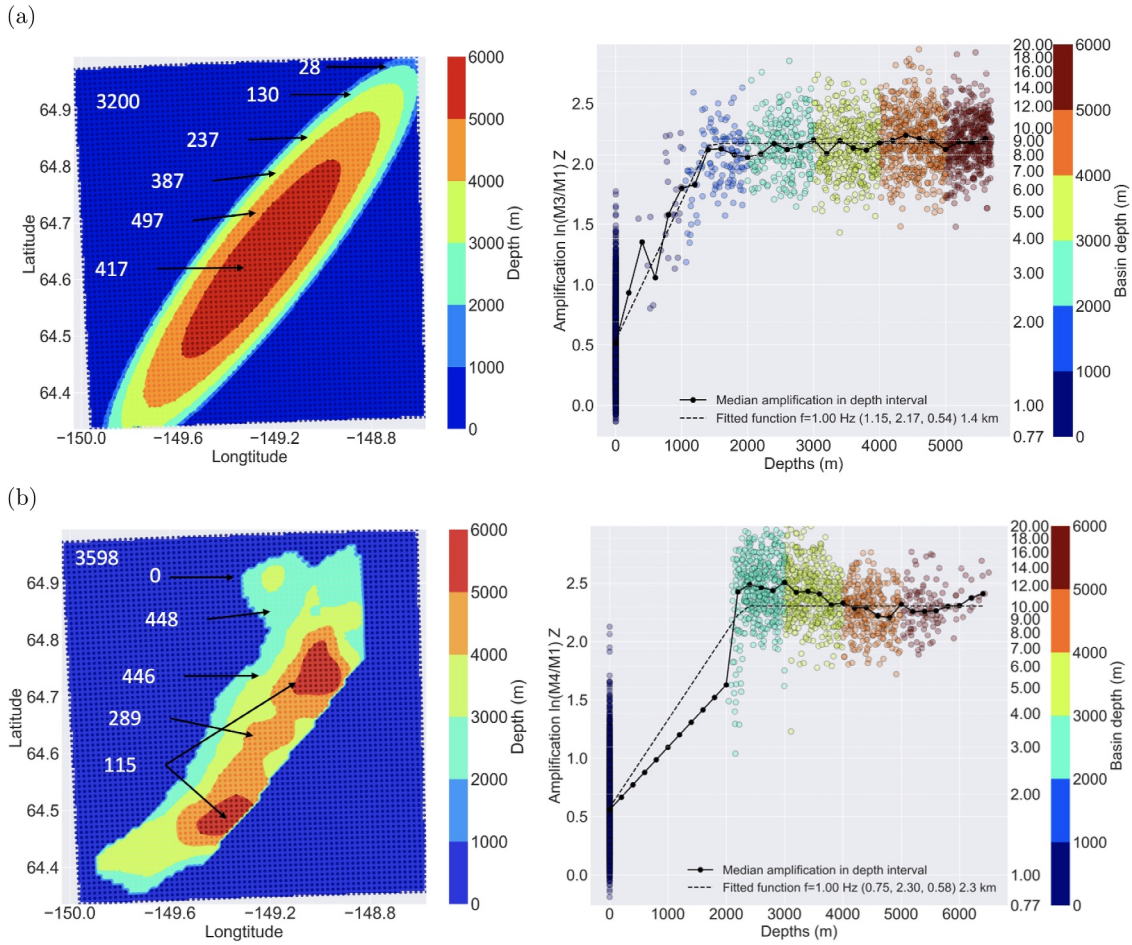

Figure 9. Basin amplification as a function of basin depth. Each of the 4,896 stations in the synthetic grid is colored according to its underlying basin depth. (a) Left: Idealized ellipsoidal basin used for seismic velocity model M3. The labeled numbers indicate the number of synthetic stations for a given depth interval. There are 1,696 stations (out of 4,896 total) inside the boundary of the M3 basin. Right: Basin amplification M3/M1 for all synthetic stations, plotted as a function of basin depth in dotted solid line. This example is calculated for a frequency of 1.00 Hz, with each dot representing the median amplification value for all 10 events (Table 1). The numbers in the legend correspond to the fitting parameters of the dashed line for the ramp-plateau functional form: 1.15 km^{-1} is slope of the ramp, 2.17 is the plateau value, 0.54 is the y-intercept, and 1.4 km is the corner depth where the ramp meets the plateau. (b) Left: Realistic basin used for seismic velocity model M4. There are 1,298 stations (out of 4,896 total) inside the boundary of the M4 basin. Right: Basin amplification M4/M1 for all synthetic stations. The gap in data is because the basin model does not have any points with depths between 0 and 2 km.

From these plots, we make the following observations:

1. Overall amplification patterns for all three components are similar for the ellipsoidal (M3) and realistic (M4) basins. There is minimal amplification at the outside-basin stations (depth 0 km), then there is a linear increase in log-scale amplification (this is only evident for M3), then there is a plateau of high amplification that generally increases with increasing frequency.
2. Basin amplification begins at about 0.025 Hz (40 s) on the horizontal components and at about 0.10 Hz (10 s) on the vertical component. We attribute this to the shallower sensitivity of Love waves, compared with Rayleigh waves, so a lower-frequency Love wave will be more sensitive to basin structure than a Rayleigh wave.
3. The corner depths of the best-fitting ramp-plateau curves decrease with increasing frequency. This occurs because higher-frequency waves are less sensitive to the deeper portions of the basin.
4. The plateau amplification value depends on frequency and component. For M3 and M4 on the vertical component, the maximal plateau amplification occurs at 0.6 Hz (1.6 s) (Figure 10a); on the horizontal component, it occurs at 0.2 Hz (5 s).
5. Amplification on the vertical component occurs at outside-basin stations (depth 0 km) for frequencies ≥0.2 Hz. By comparison, there is no amplification on the horizontal components at outside-basin stations.

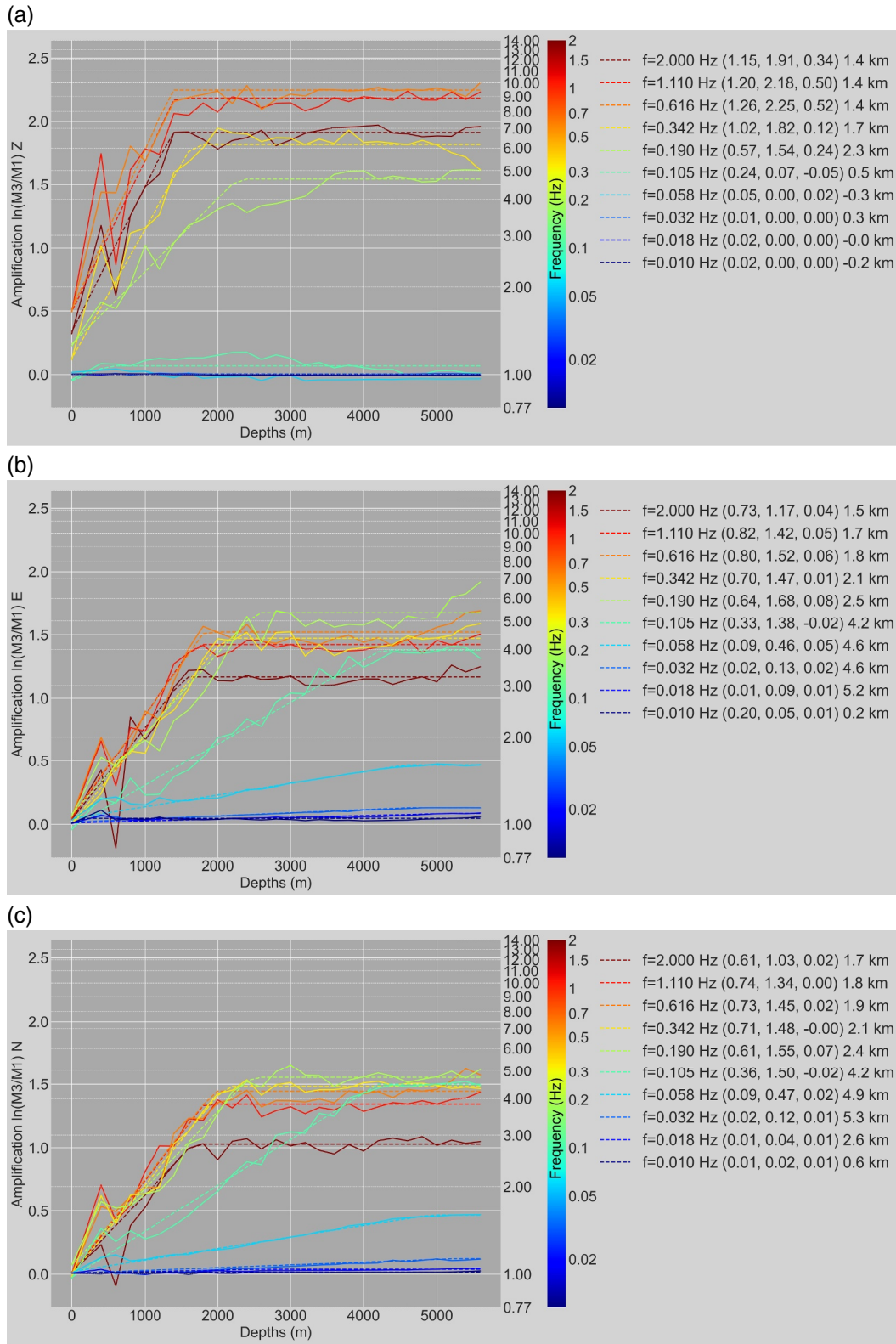

Figure 10. Basin amplification as a function of basin depth at different frequencies. The velocity model here is the ellipsoidal basin (M3); results for the realistic basin (M4) are displayed in Figure S14 in Supporting Information S1. Figure 9 illustrates how an individual curve (i.e., for a fixed frequency) is constructed. The five numbers in the legend are the frequency, the slope of the ramp (km^{-1}), the value of the plateau, the *y*-intercept, and the corner depth. See Section 3.3 for details.

6. One difference between M3 and M4 is the decrease in amplification with depths from 2 to 6 km, observed for $f > 0.2$ Hz on the vertical component for M4 (Figure S14a in Supporting Information S1; see also Figure 9b). This suggests enhanced amplification near the margin of the basin (relative to the center), but only for specific frequencies and only for the realistic basin.

3.4. Spatial Pattern of Amplification

Figure 11 provides a synoptic view of basin amplification, spanning two models (M3, M4), three components (Z, E, N), and composite results for all 10 earthquakes for the bandpass 0.1–0.5 Hz, which is the low-frequency bandpass featured in Smith et al. (2023). For each of the 4,896 synthetic stations, we calculate the broadband amplification for 0.1–0.5 Hz for 10 events and take the median value.

The dominant pattern is clear: amplification occurs inside the basin and with values of ln(M4/M1) = 1.5–2.0, corresponding to a ratio of about 5–9. We attribute the spatial variation of amplification inside the ellipsoidal basin (M3) to source mechanisms, which can be gleaned from results for each event (Tian & Tape, 2024). These general patterns are also observed in the more realistic basin (M4): amplification occurs in the northern and southern ends for the Z component, and in the northern end for the E and N components (Figure 11).

Figure 12 is an alternative representation of Figure 11, where we have used the basin depth for each station. The subplots in Figure 12 contain the same information conveyed in Figure 11, but emphasizing the basin depth for each station in the synthetic grid. The outside-basin, low-amplification, blue regions of Figure 11 collapse to the $x = 0$ portions of Figure 12, while the inside-basin, high-amplification yellow-to-red regions in Figure 11 display as the mostly-uniform amplification values for depths $x > 3000$ m in Figure 12. The inside-basin synthetic gridpoints near the margin provide insights into the transition between bedrock stations and deeper basin stations.

The basic two-segment (ramp-plateau) pattern from Figure 10 is visible for all components and for both models. The results for M4/M1 suggest a much steeper slope on the depth interval 0–2 km than the one for M3/M1 (about 2 vs. 0.75 km^{-1}); this can also be seen in the 1 Hz example in Figure 9.

The east component, especially for M3/M1 (Figure 12b), shows a bifurcation that turns out to be related to the selection of events. The upper set of points are predominantly in the northern part of the basin, where amplification is higher for these events, while the lower set of points are for the southern part of the basin (Figures S15 and S16 in Supporting Information S1). For example, the locations F1TN and F2TN are in the north and have amplifications of about 6.5, while FNN2 is in the south and has an amplification of about 4.5 (Figure 12b).

For reference, in Figure 11 we have plotted the locations of 14 stations that are within the synthetic grid: 13 FLATS (XV) stations and AK.NEA2. These stations enable comparisons between observed and simulated ground motion, discussed next.

3.5. Comparison With Observations

Thus far, our analysis has focused on synthetic seismograms only. As shown in Smith and Tape (2019b) and Smith et al. (2023), we can approximate basin amplification by using real data and choosing a nearby reference bedrock station. To compare our calculations of synthetic amplification with approximations from real data, we downloaded three-component waveforms for the 10 events listed in Table 1. We calculated spectral ratios between each station and the reference bedrock station XV.F8KN (Smith et al., 2023). We applied the same signal processing to the observed waveforms as we did to the synthetic waveforms.

Figure 12 superimposes two additional sets of points besides the 4,896 points of the synthetic grid. The first set is the amplification values at the true station locations (F1TN, F2TN, etc); these are plotted as dark blue points. Their plotted locations differ for M3 and M4, since both their amplification values and their basin depths differ. The second set is the observed amplification ratios for the same set of 10 earthquakes, as measured between the station and the reference bedrock station; these are plotted as red triangles.

From Figure 12 we provide the following remarks:

- The observations generally follow the patterns of the synthetics, having lowest values for bedrock sites and highest values for the deeper basin sites.
- The synthetic amplification values on the vertical component exceed the observations (Figures 12a and 12d).

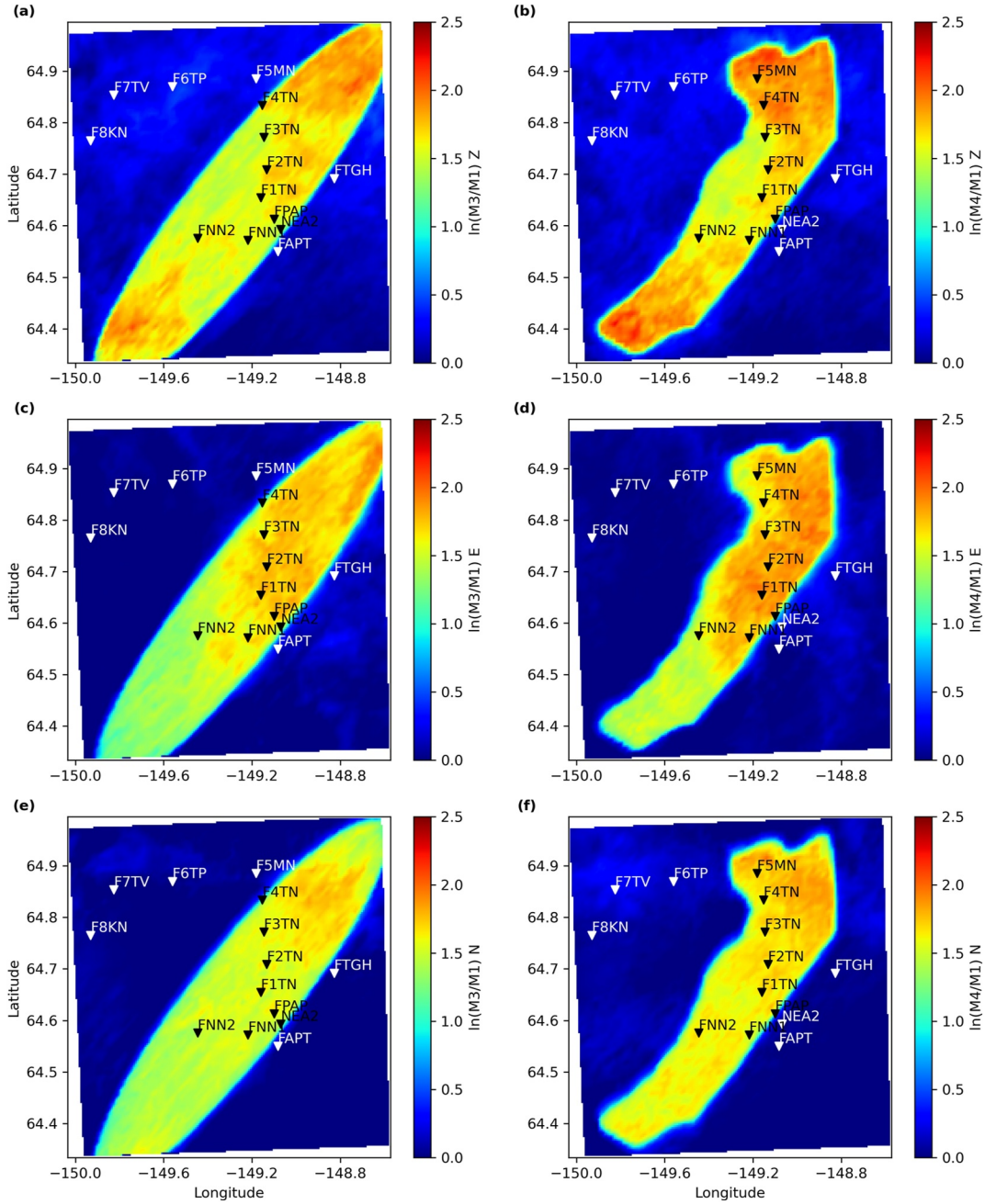

Figure 11. Spatial maps of amplification based on simulations for the 10 earthquakes listed in Table 1. The left column is for M3/M1, the right column for M4/M1. Each row is for a different component: Z (top), E (middle), and N (bottom). Amplification is calculated for the bandpass 0.1–0.5 Hz (2–10 s); the value plotted in color is the median amplification of all 10 events (Table 1). The same information here is used in the amplification-versus-depth plots in Figure 12. The real station locations are plotted for reference; see also Figure 1bc.

- Observations for northern basin stations F3TN, F4TN, and F5MN on the north component (and, to a lesser extent, the east component) exceed synthetic amplification values (Figures 12c and 12f). This suggests that in this region the true basin structure—either the geometry or the assumed velocity model—is not represented well by the ellipsoidal or realistic basin model.
- Observations for the marginal basin stations FPAP, FAPT, F6TP, and F7TV—for which a depth of 1 km has been assumed (Smith et al., 2023)—are consistent with amplification calculations for the ellipsoidal basin for

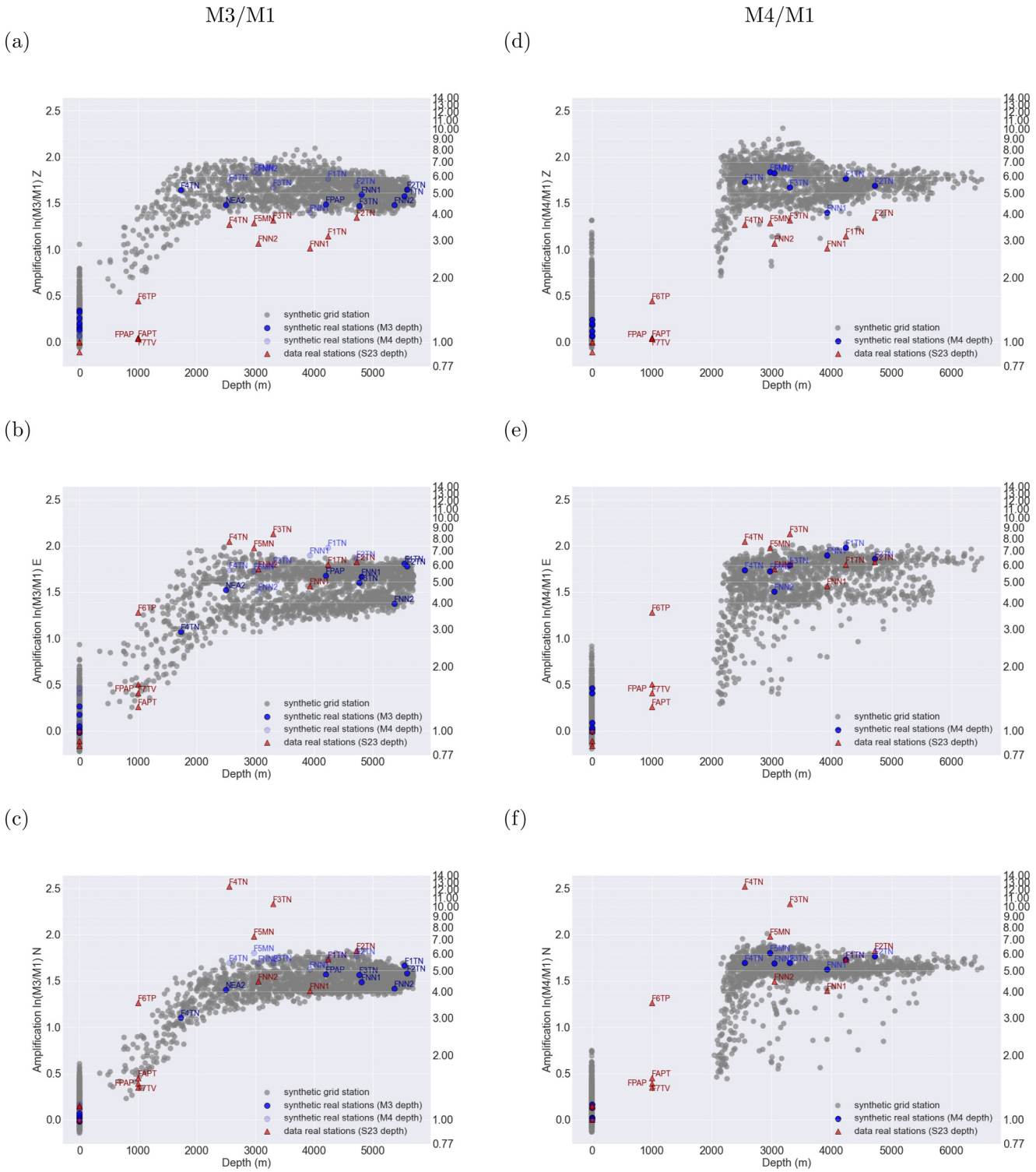

Figure 12. Comparison of basin amplification for simulations (Figure 11) and observations for a set of 10 earthquakes. The left column is for M3/M1, the right column for M4/M1. Each row is for a different component: Z (top), E (middle), and N (bottom). Amplification is calculated for the bandpass 0.1–0.5 Hz (2–10 s); the value displayed is the median amplification of all 10 earthquakes. Observations from real data are from Smith et al. (2023), but recalculated here in order to have the same processing as applied to the synthetics. The S23 depth is the M4 depth but modified according to Smith et al. (2023), with stations F6TP, F7TV, FAPT, and FPAP assigned a depth of 1 km. The locations of the light blue points at the left are identical to the dark blue points at the right, which are based on the M4 model results. See Section 3.5 for details.

the horizontal components (Figures 12b and 12c), but not for the vertical component, where the observed amplifications are less than predictions and closer in value to bedrock stations (Figure 12a).

4. Discussion and Conclusions

We are interested in how sedimentary basins amplify the seismic wavefield from local earthquakes. As conveyed in Figure 1, Nenana basin has the advantage of having relatively good station coverage (in 2014–2019) and also local earthquakes: the region hosts moderate-magnitude (M_w 4) earthquakes, from which reliable source mechanisms can be estimated. While the region has the potential for a M_w 7 earthquake (Tape et al., 2015), it does not have the urban population density that motivates studies and seismic deployments in other basins (Tokyo, Mexico City, Los Angeles, Seattle, etc). At present, there are no stations within Nenana basin, and there are no known plans for any deployment.

4.1. A General Approach to Quantifying Basin Amplification

Our study provides the third stage of investigating the influence of Nenana basin on the seismic wavefield. The approach could be applied to any basin having broadband seismic stations inside and outside the basin. These stages are:

1. Quantification of basin amplification from ambient seismic noise (Perron et al., 2018; Smith & Tape, 2019a). This requires careful consideration of the factors that contribute to seismic noise; for example, in Nenana basin, the basin noise amplification was calculated during the winter months, when the nearby Tanana River was frozen at the surface, and during time periods of no wind. This quantification does not require earthquake recordings.
2. Quantification of basin amplification from local, regional, and teleseismic earthquakes (Smith et al., 2023). By using a range of earthquakes having different magnitudes and epicentral distances, we can consider a broad range of frequencies and amplitudes of waves entering the basin. Care is needed to account for the different ray paths from each source to the basin station and from each source to the reference bedrock station, since these ray paths have different distances and different piercing points on the source mechanism.
3. Quantification of basin amplification using 3D wavefield simulations (this study). This approach has the benefit of considering any number of 3D velocity models, while also not needing any nearby reference station for comparison. Also, no recorded seismic wavefield is required.

Both the observational approaches (Stages 1 and 2) and the simulation approach (Stage 3) have limitations. The noise-based approach (Stage 1) deals with the low-amplitude ambient wavefield rather than higher-amplitude earthquake wavefields (Stage 2). Earthquake recordings include high-frequency (1–10 Hz) waveforms, yet typically the station spacing is not nearly dense enough to capture the coherent features in the wavefield. Something like the urban arrays deployed in southern California (Lin et al., 2013) would be needed to link high-frequency waveforms with structural details of the basin.

The main limitations for the simulations are twofold. First, a simulation's utility depends on the accuracy and relevance of the velocity model it employs. Second, there is always an upper frequency limit imposed by computational resources. And even with massive computational resources, it becomes questionable to pursue simulations in a realm where the important details of the velocity model (including scattering heterogeneity and attenuation) are not well known.

Our study provides general insights that were not possible in previous efforts in Nenana basin (Smith & Tape, 2019a; Smith et al., 2023). We discuss our results in the context of two simulation-based studies, Wirth et al. (2019) and Day et al. (2008).

The Seattle basin study of Wirth et al. (2019) demonstrates that the source location, depth, and mechanism can all influence ground motion amplification for a particular location within a sedimentary basin. Our results agree with this, especially for earthquakes directly below the basin, where the aperture of the source mechanism is large enough to imprint source patterns on the variations in ground motions (Figure 4). By considering real sources—having different hypocenters and mechanisms—we are able to address source variations, such as the variability shown in plots like Figure 6.

The Los Angeles basin study of Day et al. (2008) examined basin effects for periods 2–10 s using a suite of 60 scenario earthquakes having magnitudes 6.3–7.1. Their Figure 7 conveys key results: amplification increases sharply with depth to about 1 km, then increases gradually for deeper depths; and amplification increases for longer periods, with a maximum displayed at 10 s period.

By comparison with Day et al. (2008), our study considers a higher maximum frequency (2 Hz) and real, yet smaller-magnitude, earthquakes. Our two-segment model (Figure 9) is similar to the core result in Figure 7 of Day et al. (2008). One difference is that ours is flat below a frequency-dependent depth, indicating that the propagating waves are insensitive to structures at these depths. Day et al. (2008) concluded (p. 8): "Source-averaged basin amplification is period dependent, with the highest amplifications occurring for the longest periods and greatest basin depths." By comparison, our amplification values approach their peak values at a lower period of about 5 s (0.2 Hz), likely because Nenana basin is smaller than Los Angeles basin. For the vertical component, the peak amplification occurs at 0.6 Hz (1.6 s) and is sustained to 2 Hz (Figure 6). At periods longer than 40 s, no amplification occurs, since the waves are minimally sensitive to the basin (Figure 7).

We follow—and advocate—the basic approach of Day et al. (2008), which constructs source-averaged, frequency- and depth-dependent amplification curves. The outcome directly depends on the velocity model for the basin and, to a lesser extent, the sources considered. By using real earthquakes and real observations, we can better assess the validity of the simulations results.

4.2. Classical Tomography Does Not Capture Basin Details

It is well-known that classical seismic imaging, which employs ray-based approximation to the wavefield (e.g., ray paths, arrival times), produces Earth models having smoother features than the true Earth (Liu & Gu, 2012; Thurber & Ritsema, 2007). This can be partly overcome by using better data, more data, and less-approximate methods, such as adjoint methods (also known as full waveform inversion). For example, the study of Tape et al. (2010) iteratively refined a southern California velocity model to an extent that lateral surface waves in 3D wavefield simulations were reflected from the southern margin of San Joaquin basin. A more common approach is to impose higher-amplitudes and sharper contrasts in the velocity model, such as for plumes (Ni et al., 2002), slabs (Chen et al., 2007), or basins (Grapenthin et al., 2018). This manual intervention is a recognition that most tomographic models are overly smooth and cannot capture realistic, fine-scale features and contrasts.

The 3D tomographic model that we use (Berg et al., 2020) was obtained using the same stations featured in our study, as well as 200 other stations across Alaska. Therefore, the tomographic model had the potential to resolve the low velocities of Nenana basin. While it does identify a slow anomaly near the basin (Figure S1c in Supporting Information S1), it doesn't capture the details for three reasons: (a) it considers relatively long periods 8–100 s that are less sensitive to basin details, (b) it uses a coarse horizontal parameterization (0.1° latitude and 0.2° longitude, which is about 10 km), (c) it uses an approximate representation for the forward wavefield, which does not allow for iterations to obtain the strongest perturbations from the initial model.

Potentially we could have performed wavefield simulations in a 1D model (a hypothetical model M0) to demonstrate that the tomographic model (M1) exhibits minimal amplification with respect to M0. However, this could be seen from inspection of the M1 synthetic seismograms, which do not differ significantly for inside-basin and outside-basin stations. For these reasons, our preferred model M4 contains a realistic basin model embedded into a tomographic model (Section 2.1).

4.3. Basin Geometry Versus Low-Velocity Layers

Our study provides evidence for the importance of 3D basin geometry on the amplification of seismic waves. Consider the comparison M2/M1, which shows the influence of basin-like velocities in the entire uppermost 6.5 km, without any basin geometry at all. Figure 8a does not capture the details in the data (Figure 12); in fact, we would not even call this amplification, since some frequencies are amplified (with respect to M2) while others are deamplified. The same comparison of M2 and M1 also reveals that a sharp vertical contrast (here, 6.5 km depth), such as shown in Figure 3, does not cause basin amplification for the events and frequencies in our study.

The comparisons M3/M2 and M4/M2 demonstrate that the lateral basin geometry is more significant than the low-velocity layers, which is why most of our results focus on M3/M1 and M4/M1, both of which convey

amplification with respect to the tomographic model. Figure 11 shows that the key factor in amplification is whether a station is inside or outside the basin.

4.4. Consideration of Attenuation

Viscoelastic attenuation is particularly strong in sedimentary layers, especially for higher frequencies (>1 Hz) (Withers et al., 2015, 2019). Previous studies with our wave propagation solver (Specfem3d) have implemented either a constant value of attenuation within basins (Komatitsch et al., 2004; Tape et al., 2009), a V_S-to-Q_s model (Magnoni et al., 2014), or a 3D model derived from attenuation tomography (Chow et al., 2020; Savage et al., 2010).

In our study, we do not implement attenuation for the following reasons. First, we are interested in effects that are influenced by the depth of Nenana basin, which focuses our efforts on lower frequencies (0.1–0.5 Hz; Section 2.5), where attenuation effects are not as pronounced. Figure S5 in Supporting Information S1 shows a comparison of synthetic spectra for with- and without-attenuation, where attenuation was implemented using the Olsen et al. (2003) linear scaling of $Q_s = hV_S$, with h chosen to be 0.05 and V_S is in m/s. Second, there are other factors that would need to be considered, notably the attenuation model used, as well as the consideration of the source-time function for the earthquakes. We do not have any attenuation model specific for Nenana basin, so we would need to choose a generic implementation (e.g., Olsen et al., 2003). The choice of a source-time function for the simulations has the effect of filtering out higher-frequencies in the wavefield. In our simulations, we chose to set the duration of the source-time function to zero, to provide the most flexibility in post-processing. Third, our simulations with attenuation are computationally more costly by a factor of two. In summary, additional effort is needed to include attenuation within this study, and it would be particularly important if focusing on frequencies above 1 Hz.

4.5. Future Directions

We conclude with some possible future directions for this research on quantifying amplification of Nenana basin.

1. Ground motion prediction equations. Previous studies have attempted to distill basin amplification effects into empirical equations depending on the basin depth at a station and the frequency of the waves (Choi et al., 2005; Day et al., 2008; Moschetti et al., 2019). A more comprehensive set of simulations could be performed to isolate source, path, and site effects, by using observation-based approaches, such as Parker et al. (2020).
2. Basin edge effects. Previous studies have emphasized amplification effects near the edges of basins (e.g., Frankel et al., 2009; R. W. Graves et al., 1998; Kawase, 1996). Basin edges pose challenges for two reasons. First, in several models, including Nenana basin, the details near the edges are unclear. Second, even if the edges are clear, they can be challenging to adequately mesh for numerical simulations. By design (Section 2.1), our embedded Nenana basin models—either ellipsoidal (M3) or realistic (M4)—do not have any tapered structure near their edges. Future simulation efforts could consider basin models having different edge structures.
3. Improved basin models with dense deployments. In the past decade, dense seismic arrays have been used to obtain improved models of basin velocities and basin geometries, such as in southern California (Villa et al., 2023; Wang et al., 2021; Zhou & Clayton, 2024). Such efforts would be considerably more challenging in the roadless region of Nenana basin.
4. Direct comparisons of data and synthetic seismograms. Amplification calculations are based on spectral comparisons, which emphasize amplitudes. Wiggle-for-wiggle matching of recorded and simulated seismograms in sedimentary basins is a grand challenge, even for long periods (>4 s), and it becomes extremely difficult for higher frequencies (>1 Hz). At longer periods, the differences could reveal larger-scale deficiencies in the Nenana basin velocity model and its surrounding tomographic model.
5. Improved basin models with estimation techniques. The detailed wiggles in ground motion recordings from basin stations are expressions of basin structures, which, in principle, can be used to define a misfit function with modeled seismograms to iteratively improve a 3D model of the basin, as demonstrated by Iwaki and Iwata (2011) for the Osaka basin. A major challenge is that the existing station coverage becomes increasingly sparse—in terms of inter-station wavelengths—as one considers higher-frequency waveforms.

As discussed in Section 4.1, we believe our approach to characterizing basin amplification of Nenana basin could be pursued with any other reasonably well-instrumented basins. Given the extreme impact of sedimentary basins on the seismic wavefields, as well as the societal relevance of seismic hazards, it is sensible to quantify baseline amplification effects for the world's major sedimentary basins, by using a combination of observations and simulations.

Conflict of Interest

The authors declare no conflicts of interest relevant to this study.

Data Availability Statement

This study uses a suite of open-source software that can be found from the GitHub organization adjTomo (Chow, 2025), including PySEP, wfdiff, Specfem3d (Komatitsch et al., 2004; Peter et al., 2011), and SeisFlows (Chow et al., 2020). Specfem3d online tutorials are available via the SCOPED project (Denolle et al., 2025). Specfem3d input files for our study are provided in Tian and Tape (2024), which also contains details beyond those presented in the Supplement. The four seismic velocity models (Figure 2) are provided in Tian and Tape (2025b). Estimation of the minimum resolvable period is documented in Tian and Tape (2025a).

Seismic waveforms were obtained from the EarthScope Data Management Center. The stations were part of the following networks: FLATS (Tape & West, 2014; Tape et al., 2018), TA (Busby & Aderhold, 2020; IRIS, 2003), and AK (Alaska Earthquake Center, Univ. of Alaska Fairbanks, 1987).

Acknowledgments

We thank Elif Oral and Kim Olsen for their careful reviews, which improved the manuscript. We thank University of Alaska Fairbanks (UAF) Research Computing Systems for an allocation on the "chinook" high-performance computing cluster. This study is part of the SCOPED project, which is supported by Grant OAC 2104052 from the National Science Foundation. Parts of this work were performed under the auspices of the U.S. Department of Energy (DOE) by Lawrence Livermore National Laboratory (LLNL) under Contract DE-AC52-07NA27344. LLNL IM release number is LLNL-JRNL-2002946. We acknowledge helpful discussions with Kyle Smith, Victor Tsai, and Marine Denolle.

References

Alaska Earthquake Center, Univ. of Alaska Fairbanks. (1987). *Alaska geophysical network*. International Federation of Digital Seismograph Networks. Other/Seismic Network. https://doi.org/10.7914/SN/AK

Anderson, J. G., Bodin, P., Brune, J. N., Prince, J., Singh, S. K., Quaas, R., & Onate, M. (1986). Strong ground motion from the Michoacan, Mexico, earthquake. *Science*, *233*(4768), 1043–1049. https://doi.org/10.1126/science.233.4768.1043

Asano, K., Sekiguchi, H., Iwata, T., Yoshimi, M., Hayashida, T., Saomoto, H., & Horikawa, H. (2016). Modelling of wave propagation and attenuation in the Osaka sedimentary basin, western Japan, during the 2013 Awaji Island earthquake. *Geophysical Journal International*, *204*(3), 1678–1694. https://doi.org/10.1093/gji/ggv543

Bard, P.-Y., & Bouchon, M. (1980). The seismic response of sediment-filled valleys. Part 1. The case of incident *SH* waves. *Bulletin of the Seismological Society of America*, *70*(4), 1263–1286. https://doi.org/10.1785/bssa0700041263

Bard, P.-Y., & Bouchon, M. (1985). The two-dimensional resonance of sediment-filled valleys. *Bulletin of the Seismological Society of America*, *75*(2), 519–541. https://doi.org/10.1785/bssa0750020519

Bard, P.-Y., Campillo, M., Chávez-Garcia, F. J., & Sánchez-Sesma, F. (1988). The Mexico earthquake of September 19, 1985—A theoretical investigation of large- and small-scale amplification effects in the Mexico City valley. *Earthquake Spectra*, *4*(3), 609–633. https://doi.org/10.1193/1.1585493

Berg, E. M., Lin, F.-C., Allam, A., Schulte-Pelkum, V., Ward, K. M., & Shen, W. (2020). Shear velocity model of Alaska via joint inversion of Rayleigh wave ellipticity, phase velocities, and receiver functions across the Alaska Transportable Array. *Journal of Geophysical Research: Solid Earth*, *125*(2), e2019JB018582. https://doi.org/10.1029/2019JB018582

Bonilla, L. F., Steidl, J. H., Lindley, G. T., Tumarkin, A. G., & Archuleta, R. J. (1997). Site amplification in the San Fernando Valley, California: Variability of site-effect estimation using the S-Wave, coda, and H/V methods. *Bulletin of the Seismological Society of America*, *87*(3), 710–730. https://doi.org/10.1785/bssa0870030710

Brocher, T. M. (2008). Compressional and shear-wave velocity versus depth relations for common rock types in northern California. *Bulletin of the Seismological Society of America*, *98*(2), 950–968. https://doi.org/10.1785/0120060403

Busby, R. W., & Aderhold, K. (2020). The Alaska transportable array: As built. *Seismological Research Letters*, *91*(6), 3017–3027. https://doi.org/10.1785/0220200154

Chen, M., Tromp, J., Helmberger, D., & Kanamori, H. (2007). Waveform modeling of the slab beneath Japan. *Journal of Geophysical Research*, *112*(B2), 1–19. https://doi.org/10.1029/2006JB004394

Choi, Y., Stewart, J. P., & Graves, R. W. (2005). Empirical model for basin effects accounts for basin depth and source location. *Bulletin of the Seismological Society of America*, *95*(4), 1412–1427. https://doi.org/10.1785/0120040208

Chow, B. (2025). adjTomo. Retrieved from https://github.com/adjtomo/

Chow, B., Kaneko, Y., Tape, C., Modrak, R., & Townend, J. (2020). An automated workflow for adjoint tomography—Waveform misfits and synthetic inversions for the North Island, New Zealand. *Geophysical Journal International*, *223*(3), 1461–1480. https://doi.org/10.1093/gji/ggaa381

Cruz-Atienza, V. M., Tago, J., Sanabria-Gómez, J. D., Chaljub, E., Etienna, V., Virieux, J., & Quintanar, L. (2016). Long duration of ground motion in the paradigmatic Valley of Mexico. *Scientific Reports*, *6*, 1–9. https://doi.org/10.1038/srep38807

Day, S. M., Graves, R., Bielak, J., Dreger, D., Larsen, S., Olsen, K. B., et al. (2008). Model for basin effects on long-period response spectra in southern California. *Earthquake Spectra*, *24*(1), 257–277. https://doi.org/10.1193/1.2857545

Denolle, M., Tape, C., Bozdağ, E., Wang, Y., Waldhauser, F., Gabriel, A.-A., et al. (2025). Training the next generation of seismologists: Delivering research-grade software education for Cloud and HPC computing through diverse training modalities. *Seismological Research Letters*, *96*(5), 3265–3279. https://doi.org/10.1785/0220240413

Dixit, N., Hanks, C., Rizzo, A., McCarthy, P., & Coakley, B. (2017). Cenozoic tectonic and thermal history of the Nenana basin, central interior Alaska: New constraints from seismic reflection data, fracture history, and apatite fission-track analyses. *Canadian Journal of Earth Sciences*, *54*(7), 766–784. https://doi.org/10.1139/cjes-2016-0197

Frankel, A. (1993). Three-dimensional simulations of ground motions in the San Bernadino Valley, California, for hypothetical earthquakes on the San Andreas Fault. *Bulletin of the Seismological Society of America*, *83*(4), 1020–1041. https://doi.org/10.1785/bssa0830041020

Frankel, A., Stephenson, W., & Carver, D. (2009). Sedimentary basin effects in Seattle, Washington: Ground-motion observations and 3D simulations. *Bulletin of the Seismological Society of America*, *99*(3), 1579–1611. https://doi.org/10.1785/0120080203

Furumura, T., & Koketsu, K. (1998). Specific distribution of ground motion during the 1995 Kobe earthquake and its generation mechanism. *Geophysical Research Letters*, *25*(6), 785–788. https://doi.org/10.1029/98gl50418

Galetzka, J., Melgar, D., Genrich, J. F., Geng, J., Owen, S., Lindsey, E. O., et al. (2015). Slip pulse and resonance of the Kathmandu basin during the 2015 Gorkha earthquake, Nepal. *Science*, *349*(6252), 1091–1095. https://doi.org/10.1126/science.aac6383

Grapenthin, R., West, M., Tape, C., Gardine, M., & Freymueller, J. (2018). Single-frequency instantaneous GNSS velocities resolve dynamic ground motion of the 2016 Mw 7.1 Iniskin, Alaska, earthquake. *Seismological Research Letters*, *89*(3), 1040–1048. https://doi.org/10.1785/0220170235

Graves, R., & Pitarka, A. (2016). Kinematic ground-motion simulations on rough faults including effects of 3D stochastic velocity perturbations. *Bulletin of the Seismological Society of America*, *106*(5), 2136–2153. https://doi.org/10.1785/0120160088

Graves, R. W., Pitarka, A., & Somerville, P. G. (1998). Ground-motion amplification in Santa Monica area: Effects of shallow basin-edge structure. *Bulletin of the Seismological Society of America*, *88*(5), 1224–1242. https://doi.org/10.1785/bssa0880051224

IRIS. (2003). *USArray transportable array*. International Federation of Digital Seismograph Networks. Other/Seismic Network. https://doi.org/10.7914/SN/TA

Iwaki, A., & Iwata, T. (2011). Estimation of three-dimensional boundary shape of the Osaka sedimentary basin by waveform inversion. *Geophysical Journal International*, *186*(3), 1255–1278. https://doi.org/10.1111/j.1365-246X.2011.05102.x

Kawase, H. (1996). The cause of the damage belt in Kobe: "The basin-edge effect," constructive interference of the direct S-wave with the basin-induced diffracted/Rayleigh waves. *Seismological Research Letters*, *67*(5), 25–34. https://doi.org/10.1785/gssrl.67.5.25

Kawase, H. (2003). Site effects on strong ground motions. In W. H. K. Lee, H. Kanamori, P. C. Jennings, & C. Kisslinger (Eds.), *International handbook of earthquake and engineering seismology* (Vol. 81B, pp. 1013–1030). Academic Press.

Koehler, R. D., Farrell, R.-E., Burns, P. A. C., & Combellick, R. A. (2012). *Quaternary faults and folds in Alaska: A digital database* (Vol. 141, p. 31). Alaska Division of Geological & Geophysical Surveys Miscellaneous Publication. 1, scale 1:3,700,000. https://doi.org/10.14509/23944

Komatitsch, D., Liu, Q., Tromp, J., Süss, P., Stidham, C., & Shaw, J. H. (2004). Simulations of ground motion in the Los Angeles basin based upon the spectral-element method. *Bulletin of the Seismological Society of America*, *94*(1), 187–206. https://doi.org/10.1785/0120030077

Komatitsch, D., Ritsema, J., & Tromp, J. (2002). The spectral-element method, Beowulf computing, and global seismology. *Science*, *298*(5599), 1737–1742. https://doi.org/10.1126/science.1076024

Lee, S.-J., Chen, H.-W., Liu, Q., Komatitsch, D., Huang, B.-S., & Tromp, J. (2008). Three-dimensional simulations of seismic-wave propagation in the Taipei basin with realistic topography based upon the spectral-element method. *Bulletin of the Seismological Society of America*, *98*(1), 253–264. https://doi.org/10.1785/0120070033

Lin, F.-C., Li, D., Clayton, R. W., & Hollis, D. (2013). High-resolution 3D shallow crustal structure in Long Beach, California: Application of ambient noise tomography on a dense seismic array. *Geophysics*, *78*(4), Q45–Q56. https://doi.org/10.1190/geo2012-0453.1

Liu, Q., & Gu, Y. J. (2012). Seismic imaging: From classical to adjoint tomography. *Tectonophysics*, *566–567*, 31–66. https://doi.org/10.1016/j.tecto.2012.07.006

Magnoni, F., Casarotti, E., Michelini, A., Piersanti, A., Komatitsch, D., Peter, D., & Tromp, J. (2014). Spectral-element simulations of seismic waves generated by the 2009 L'Aquila earthquake. *Bulletin of the Seismological Society of America*, *104*(1), 73–94. https://doi.org/10.1785/0120130106

Mayoral, J. M., nd, S., Tepalcapa, D. A., Wood, C., Roman-de la Sancha, A., Hutchinson, T., et al. (2019). Site effects in Mexico City basin: Past and present. *Soil Dynamics and Earthquake Engineering*, *121*, 369–382. https://doi.org/10.1016/j.soildyn.2019.02.028

Moschetti, M. P., Thompson, E. M., Rekoske, J., Hearne, M. G., Powers, P. M., McNamara, D., & Tape, C. (2019). Ground-motion amplification in Cook Inlet Region, Alaska from intermediate-depth earthquakes, including the 2018 Mw7.1 Anchorage earthquake. *Seismological Research Letters*, *91*(1), 142–152. https://doi.org/10.1785/0220190179

Ni, S., Tan, E., Gurnis, M., & Helmberger, D. (2002). Sharp sides to the African superplume. *Science*, *296*(5574), 1850–1852. https://doi.org/10.1126/science.1070698

Olsen, K. B. (2000). Site amplification in the Los Angeles basin from three-dimensional modelling of ground motion. *Bulletin of the Seismological Society of America*, *60*(6B), S77–S94. https://doi.org/10.1785/0120000506

Olsen, K. B., Archuleta, R. J., & Matarese, J. R. (1995). Three-dimensional simulation of a magnitude 7.75 earthquake on the San Andreas Fault. *Science*, *270*(5242), 1628–1632. https://doi.org/10.1126/science.270.5242.1628

Olsen, K. B., Day, S. M., & Bradley, C. R. (2003). Estimation of Q for long-period (>2 sec) waves in the Los Angeles basin. *Bulletin of the Seismological Society of America*, *93*(2), 627–638.

Oral, E., Ayoubi, P., Ampuero, J. P., Asimaki, D., & Bonilla, L. F. (2022). Kathmandu Basin as a local modulator of seismic waves: 2-D modelling of non-linear site response under obliquely incident waves. *Geophysical Journal International*, *231*(3), 1996–2008. https://doi.org/10.1093/gji/ggac302

Parker, G. A., Baltay, A. S., Rekoske, J., & Thompson, E. M. (2020). Repeatable source, path, and site effects from the 2019 M 7.1 Ridgecrest earthquake sequence. *Bulletin of the Seismological Society of America*, *110*(4), 1530–1548. https://doi.org/10.1785/0120200008

Perron, V., Gélis, C., B. Froment, B., Hollender, F., Bard, P.-Y., Cultrera, G., & Cushing, E. M. (2018). Can broad-band earthquake site responses be predicted by the ambient noise spectral ratio? Insight from observations at two sedimentary basins. *Geophysical Journal International*, *215*, 1442–1454. https://doi.org/10.1093/gji/ggy355

Peter, D., Komatitsch, D., Luo, Y., Martin, R., Le Goff, N., Casarotti, E., et al. (2011). Forward and adjoint simulations of seismic wave propagation on fully unstructured hexahedral meshes. *Geophysical Journal International*, *186*(2), 721–739. https://doi.org/10.1111/j.1365-246x.2011.05044.x

PRA. (2017). *Depth to basement map of Nenana Basin, Alaska*. Petrotechnical Resources of Alaska.

Sánchez-Sesma, F., & Luzón, F. (1995). Seismic response of three-dimensional alluvial valleys for incident P, S, and Rayleigh waves. *Bulletin of the Seismological Society of America*, *85*(1), 269–284.

Savage, B., Komatitsch, D., & Tromp, J. (2010). Effects of 3D attenuation on seismic wave amplitude and phase measurements. *Bulletin of the Seismological Society of America*, *100*(3), 1241–1251. https://doi.org/10.1785/0120090263

Savran, W. H., & Olsen, K. B. (2016). Model for small-scale crustal heterogeneity in Los Angeles basin based on inversion of sonic log data. *Geophysical Journal International*, *205*(2), 856–863. https://doi.org/10.1093/gji/ggw050

Shaw, J. H., Plesch, A., Tape, C., Suess, M. P., Jordan, T. H., Ely, G., et al. (2015). Unified structural representation of the southern California crust and upper mantle. *Earth and Planetary Science Letters*, *415*, 1–15. https://doi.org/10.1016/j.epsl.2015.01.016

Sims, N. E., Tape, C., Ruppert, N. A., & West, M. E. (2025). High precision earthquake catalog for Minto Flats fault zone, central Alaska, reveals complex and conjugate faulting. *Bulletin of the Seismological Society of America*. https://doi.org/10.1785/0120250177

Smith, K., & Tape, C. (2019a). Seismic noise in central Alaska and influences from rivers, wind, and sedimentary basins. *Journal of Geophysical Research: Solid Earth*, *124*(11), 11678–11704. https://doi.org/10.1029/2019JB017695

Smith, K., & Tape, C. (2019b). Seismic response of Cook Inlet sedimentary basin, southern Alaska. *Seismological Research Letters*, *91*(1), 33–55. https://doi.org/10.1785/0220190205

Smith, K., Tape, C., & Tsai, V. C. (2023). Seismic response of Nenana sedimentary basin, central Alaska. *Bulletin of the Seismological Society of America*, *113*(2), 762–781. https://doi.org/10.1785/0120220160

Stupazzini, M., Paolucci, R., & Igel, H. (2009). Near-fault earthquake ground-motion simulation in the Grenoble Valley by a high-performance spectral element code. *Bulletin of the Seismological Society of America*, *99*(1), 286–301. https://doi.org/10.1785/0120080274

Süss, M. P., & Shaw, J. H. (2003). P-wave seismic velocity structure derived from sonic logs and industry reflection data in the Los Angeles basin, California. *Journal of Geophysical Research*, *108*(B3). https://doi.org/10.1029/2001JB001628

Tape, C., Holtkamp, S., Silwal, V., Hawthorne, J., Kaneko, Y., Ampuero, J. P., et al. (2018). Earthquake nucleation and fault slip complexity in the lower crust of central Alaska. *Nature Geoscience*, *11*(7), 536–541. https://doi.org/10.1038/s41561-018-0144-2

Tape, C., Liu, Q., Maggi, A., & Tromp, J. (2009). Adjoint tomography of the southern California crust. *Science*, *325*(5943), 988–992. https://doi.org/10.1126/science.1175298

Tape, C., Liu, Q., Maggi, A., & Tromp, J. (2010). Seismic tomography of the southern California crust based on spectral-element and adjoint methods. *Geophysical Journal International*, *180*(1), 433–462. https://doi.org/10.1111/j.1365-246X.2009.04429.x

Tape, C., Silwal, V., Ji, C., Keyson, L., West, M. E., & Ruppert, N. (2015). Transtensional tectonics of the Minto Flats fault zone and Nenana basin, central Alaska. *Bulletin of the Seismological Society of America*, *105*(4), 2081–2100. https://doi.org/10.1785/0120150055

Tape, C., & West, M. E. (2014). *Fault locations and Alaska tectonics from seismicity*. International Federation of Digital Seismograph Networks. Other/Seismic Network. https://doi.org/10.7914/SN/XV_2014

Thurber, C., & Ritsema, J. (2007). Seismic tomography and inverse methods. In B. Romanowicz & A. Dziewonski (Eds.), *Seismology and structure of the Earth* (Vol. 1, pp. 323–360). Elsevier. https://doi.org/10.1016/b978-044452748-6.00009-2

Tian, Y., & Tape, C. (2024). Documentation and digital files in support of "Analysis of seismic wave amplification in sedimentary basins using 3D wavefield simulations" [Dataset]. *Zenodo*. https://doi.org/10.5281/zenodo.14284570

Tian, Y., & Tape, C. (2025a). Quantifying the minimum resolvable period in "Analysis of seismic wave amplification in sedimentary basins using 3D wavefield simulations" [Dataset]. *Zenodo*. https://doi.org/10.5281/zenodo.16331262

Tian, Y., & Tape, C. (2025b). Seismic velocity models used in "Analysis of seismic wave amplification in sedimentary basins using 3D wavefield simulations" [Dataset]. *Zenodo*. https://doi.org/10.5281/zenodo.15014279

Van Kooten, G. K., Richter, M., & Zippi, P. A. (2012). Alaska's Interior rift basins: A new Frontier for discovery. *Oil & Gas Journal*, *110*(1a), 48–57.

Villa, V., Li, Y., Clayton, R. W., & Persaud, P. (2023). Three-dimensional basin depth map of the northern Los Angeles basins from gravity and seismic measurements. *Journal of Geophysical Research: Solid Earth*, *128*(7), 1–13. https://doi.org/10.1029/2022JB025425

Wang, X., Zhan, Z., Zhong, M., Persaud, P., & Clayton, R. W. (2021). Urban basin structure imaging based on dense arrays and Bayesian array-based coherent receiver functions. *Journal of Geophysical Research: Solid Earth*, *126*(9), 1–16. https://doi.org/10.1029/2021JB022279

Wirth, E. A., Vidale, J. E., Frankel, A. D., Pratt, T. L., Marafi, N. A., Thompson, M., & Stephenson, W. J. (2019). Source-dependent amplification of earthquake ground motions in deep sedimentary basins. *Geophysical Research Letters*, *46*(12), 6443–6450. https://doi.org/10.1029/2019GL082474

Withers, K. B., Olsen, K. B., & Day, S. M. (2015). Memory-efficient simulation of frequency-dependent Q. *Bulletin of the Seismological Society of America*, *105*(6), 3129–3142. https://doi.org/10.1785/0120150020

Withers, K. B., Olsen, K. B., Day, S. M., & Shi, Z. (2019). Ground motion and intraevent variability from 3d deterministic broadband (0–7.5 Hz) simulations along a nonplanar strike-slip fault. *Bulletin of the Seismological Society of America*, *109*(1), 229–250. https://doi.org/10.1785/0120180006

Zhou, C., & Clayton, R. W. (2024). Imaging the northern Los Angeles Basins with autocorrelations. *Seismological Research Letters*. https://doi.org/10.1785/0220240140